MASTERARBEIT | MASTER'S THESIS

Titel | Title

Effect of Oxaliplatin on TLR4 Activation in Colon Carcinoma

verfasst von | submitted by

Nada Elmenofi BSc

angestrebter akademischer Grad | in partial fulfilment of the requirements for the degree of

Magistra pharmaciae (Mag. pharm.)

Wien | Vienna, 2026

Studienkennzahl lt. Studienblatt | Degree programme code as it appears on the student record sheet:	UA 066 605
Studienrichtung lt. Studienblatt | Degree programme as it appears on the student record sheet:	Masterstudium Pharmazie
Betreut von | Supervisor:	Univ.-Prof. Dipl.-Ing. Dr. Manfred Ogris
Mitbetreut von | Co-Supervisor:	Haider Sami Ph.D.

Acknowledgements

I would like to express my sincere gratitude to Univ. Prof. Manfred Ogris for giving me the opportunity to work in his department in the MMCT-laboratory. I am truly thankful for the experience and the knowledge I was able to gain during my time there.

I would also like to extend my appreciation to Dr. Haider Sami for his co-supervision. His supportive, friendly, and professional manner made a significant difference, especially during challenging times. He was always approachable, helpful, and willing to provide guidance whenever needed.

My special thanks go to Mag. pharm. Marlene Eder, who has accompanied and supported me throughout my journey. She has always shown great dedication, kindness, and motivation. Even when I made mistakes, she remained patient and encouraging, always helping me find a solution and learn from the experience.

Finally, I would like to thank my family—my parents, Mona and Ramadan, my siblings Ahmad, Salma, and Tarek, as well as my nephews and my niece, Sulaiman, Amina, Ibrahim, and Rayan. Their continuous support, encouragement, and belief in me have shaped me into the person I am today and have been invaluable throughout my journey.

Table of Contents

1 Abbreviations

AB – Antibody

BALB/c - Bagg Albino mouse strain

CRC - Colorectal carcinoma

DAMPs - Damage-associated molecular patterns

ER - Endoplasmic reticulum

H&E- Hematoxylin and eosin

HIF-1- Hypoxia-inducible factor 1

HRE - Hypoxia response element

HRP - Horseradish peroxidase

HSP - Heat shock proteins

IHC - Immunohistochemistry

IKK - IκB kinase

INF - Interferon

IRAK2 - Interleukin-1 receptor-associated kinase 2

IRF3 - Interferon regulatory factor 3

Iso-Ctrl - Isotype control

LBP - Lipopolysaccharide-binding protein

LPS - Lipopolysaccharide

MAPK - Mitogen-activated protein kinase

MD-2 - Myeloid differentiation factor 2

MyD88 - Myeloid differentiation primary response protein 88

NFkB - Nuclear factor kappa B

PAMP - Pathogen-associated molecular patterns

prim. AB - Primary antibody

PRR - Pattern recognition receptor

Sec. AB - Secondary antibody

TAK1 - Transforming growth factor beta-activated kinase 1

TIR - Toll/interleukin-1 receptor domain

TIRAP - Toll/interleukin-1 receptor domain-containing adapter protein

TLR4 - Toll-like receptor 4

TRAF6 - TNF receptor-associated factor 6

TRAM1 - TRIF-related adapter molecule 1

TRIF - TIR-domain-containing adapter-inducing interferon-β

2 Abstract

Colorectal cancer remains one of the leading causes of cancer-related mortality worldwide, and despite advances in treatment strategies, therapeutic resistance and tumor progression remain major challenges. Increasing evidence suggests that inflammatory signaling pathways, especially those mediated by TLR4, play a crucial role in tumor development, progression, and response to chemotherapy.

This study investigates if the chemotherapeutic agent oxaliplatin affects TLR4 signaling in the murine colorectal cancer cell line CT26 in vitro and in vivo in a model of peritoneal carcinomatosis, with a particular focus on its key downstream mediators TRAM1, MyD88 and NFkB. Expression patterns of these three targets in healthy tissue, tumor regions, and transition zones were studied in the absence of treatment and after oxaliplatin administration. A syngeneic mouse model using luciferase marked CT26 colorectal carcinoma cells was used to investigate tumor development and protein expression in pancreatic tissues and tumor nodules. In parallel, 3D spheroid cultures derived from CT26-Luc cells were utilized to mimic the tumor microenvironment in vitro and assess treatment responses under controlled conditions. Oxaliplatin was administered at defined concentrations in both systems. Histological and immunohistochemical analyses were conducted to evaluate tissue morphology and protein expression.

The results indicate that NFkB expression in cells and tissues evaluated in this study is generally low and shows no clear activation pattern after oxaliplatin treatment. TRAM1 expression was consistently absent in tumor regions but present in healthy tissue. MyD88 expression was barely detectable across all samples. Importantly, no significant differences were observed between treated and untreated groups for any of the investigated proteins, indicating that oxaliplatin may not directly modulate TLR4 signaling in the examined context.

3 Zusammenfassung

Darmkrebs ist nach wie vor weltweit eine der häufigsten Ursachen für krebsbedingte Todesfälle, und trotz fortschrittlicher Behandlungsstrategien stellen Therapieresistenz und Tumorprogression weiterhin große Herausforderungen dar. Immer mehr Hinweise deuten darauf hin, dass entzündliche Signalwege, insbesondere solche, die durch TLR4 gesteuert werden, eine entscheidende Rolle bei der Tumorentstehung, dem Tumorfortschritt und dem Ansprechen auf eine Chemotherapie spielen.

Diese Studie untersucht, ob das Chemotherapeutikum Oxaliplatin die TLR4-Signalübertragung in der murinen Darmkrebszelllinie CT26 in vitro und in vivo in einem Modell der Peritonealkarzinose beeinflusst, wobei ein besonderer Schwerpunkt auf den wichtigsten nachgeschalteten Mediatoren TRAM1, MyD88 und NFkB liegt. Die Expressionsmuster dieser drei Zielmoleküle in gesundem Gewebe, Tumorregionen und Übergangszonen wurden ohne Behandlung sowie nach Oxaliplatin-Gabe untersucht. Ein syngenes Mausmodell unter Verwendung von Luciferase markierten CT26-Kolorektalkarzinomzellen wurde eingesetzt, um die Tumorentwicklung und Proteinexpression in Pankreasgewebe und Tumorknoten zu untersuchen. Parallel dazu wurden 3D-Sphäroidkulturen aus CT26-Luc-Zellen genutzt, um die Tumormikroumgebung in vitro nachzubilden und das Ansprechen auf die Behandlung unter kontrollierten Bedingungen zu bewerten. Oxaliplatin wurde in beiden Systemen in definierten Konzentrationen verabreicht. Zur Bewertung der Gewebemorphologie und Proteinexpression wurden histologische und immunhistochemische Analysen durchgeführt.

Die Ergebnisse zeigen, dass die NFkB-Expression in den in dieser Studie untersuchten Zellen und Geweben im Allgemeinen gering ist und nach einer Oxaliplatin-Behandlung kein eindeutiges Aktivierungsmuster aufweist. Die TRAM1-Expression fehlte in den Tumorregionen, war jedoch im gesunden Gewebe vorhanden. Die MyD88-Expression war in allen Proben kaum nachweisbar. Wichtig ist, dass bei keinem der untersuchten Proteine signifikante Unterschiede zwischen der behandelten und der unbehandelten

Gruppe festgestellt wurden, was darauf hindeutet, dass Oxaliplatin die TLR4-Signalübertragung im untersuchten Kontext möglicherweise nicht direkt moduliert.

4 Introduction

4.1 Colon Cancer

Colorectal cancer is one of the most common malignancies worldwide and represents a major cause of cancer-related mortality. In the European Union alone, more than 350,000 new cases are diagnosed each year, making it one of the three most frequently occurring cancers. Despite advances in diagnosis and treatment, colorectal cancer remains a significant health burden, although five-year survival rates have improved to approximately 55–60% in Europe. Various therapeutic approaches have been developed beyond surgery, including monoclonal antibodies such as cetuximab and bevacizumab, as well as cytotoxic agents like 5-fluorouracil, capecitabine, irinotecan, and oxaliplatin and the list goes on. (Jesus C. Fabregas, 2022)

4.2 Development of Colon Cancer on a molecular basis

In order to be able to understand the different approaches of colon carcinoma treatment, one must comprehend the development of this disease. The progression of colorectal cancer is a multi-stage process which happens over many years, caused by a series of genetic errors. This process primarily impacts two key gene classes: firstly tumor-suppressor genes, and secondly proto-oncogenes.

One of the initial steps is the inactivation of both alleles of the APC tumor-suppressor gene, located on chromosome 5q. When inherited mutations affect this gene, they cause familial adenomatous polyposis. This process is characterized by the development of hundreds to thousands of polyps in the colon, which nearly always progress to cancer when left untreated.

In addition to that, mutations in the K-Ras proto-oncogene also frequently occur. In the later stages the deletion of a portion of chromosome 18q happens, which harbors several tumor-suppressor genes like DCC, DPC4, and MADR2. These genes are part of the TGF-β signaling pathway, and their loss is linked to a very dangerous prognosis for patients. Also very frequent is a mutation in

the p53 gene on chromosome 17p, which allows cancerous cells to evade normal cell-cycle checkpoints and avoid apoptosis. As a result, these types of mutations promote the inflammatory action of the immune system that cause the uncontrolled growth of cancer cells. (Nelleke P. M. Brouwer, 2018)

4.2.1 Role of TLR4 in colon cancer

As already mentioned above, there are already different approaches considering the therapy of colorectal carcinoma. From chemotherapy and surgery to immunotherapy treatment. In this thesis, the focus is mostly on chemotherapy, specifically with oxaliplatin and its effect on the TLR4 pathway.

It has been found that TLR4 is overly expressed in colon cancer cells in humans and mice. The overexpression of this receptor is also considered to cause poor prognosis in CRC, since it activates pro-inflammatory proteins such as NFkB, MAPK, and INF, that cause the activation of transcription factors, chemokines and cytokines. As a result, this process expands cancerous cells. Therefore, researchers emphasize the usage of drugs or compounds that modify the TLR4 pathway in order to prevent or improve the diagnosis of CRC. There are already findings that prove this approach in breast cancer therapy. For example, Rajput et al. investigated the relationship between TLR4 expression and paclitaxel resistance in breast cancer cell lines with either reduced or increased TLR4 levels. They discovered that while paclitaxel destroys cancer cells, it can also activate the TLR4 pathway, which promotes tumor cell survival. These findings suggest that inhibiting TLR4 could greatly enhance the effectiveness of paclitaxel treatment. (Sandeep Rajput, 2013) (Ting-Ting Li, 2014)

4.2.1.1 TLR4

The TLR4 belongs to the family of the type 1 transmembrane proteins which are a panel of so-called pattern-recognition receptors (PRR), whose main job is to recognize pathogen-associated molecular patterns (PAMP) in mostly bacteria in order to activate a response in the immune system.

The main function of the TLR4 is to be activated by lipopolysaccharides (LPS), the key component of gram-negative bacteria. In addition to binding LPS, TLR4 can also recognize other molecules, including fusion proteins from respiratory syncytial virus, envelope proteins from mouse mammary tumor virus, pneumolysin from Streptococcus pneumoniae, and the plant-derived drug paclitaxel. However, the structural details of how these ligands interact with TLR4 are still unknown. (Taro Kawai, 2010)

The structure of TLR4 is as follows as in **Figure 1** visible:

1. In the extracellular domain there is a leucine-rich repeat (LRR) pattern
2. Furthermore, an intracellular domain that is connected to the extracellular domain by the so-called toll/interleukin-1 Receptor (TIR), which is involved in signal transduction. (Anna Stierschneider, 2023)

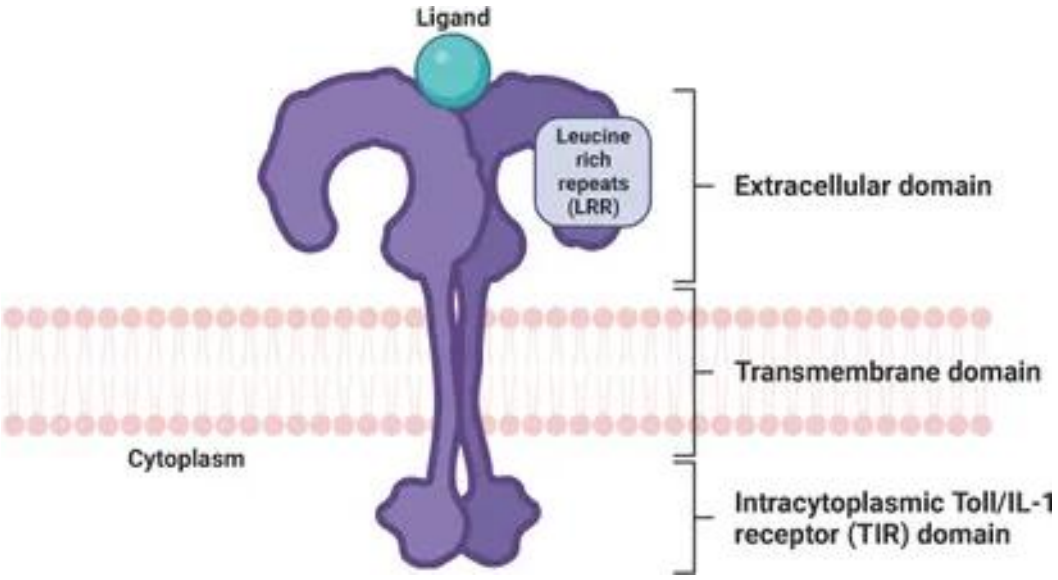

Figure 1 Conserved structure of TLRs *(Anna Stierschneider, 2023)*

4.2.1.2 The Signal Transmission of TLR4 and its key components

The signal cascade starts with the dimerization of the TLR4 (**Figure 2**) once a LPS is recognized on the surface area of this receptor (extracellular domain). Here it is important to state that the TLR4 does not directly bind with the LPS, as it needs an adapter protein. In this case it is the MD-2, the lymphocyte antigen 96. This antigen is responsible for recognizing the LPS of foreign bodies and binding it with the help of LPS-binding proteins (LBP). To make the

binding with the MD-2 possible, the LPB must take only one monomer of the LPS aggregates in solution. Once this step is completed, the LBP takes the monomer to the cluster of differentiation 14 (CD14). This protein finally delivers LPS to the MD-2 complex, which triggers the intracellular response of the TLR4 pathway. CD14 is found mostly on macrophages and monocytes and exists in two forms: soluble and membrane bound.

However, there are two different intracellular pathways from which the extracellular signal can be transmitted to: The TLR4-MyD88-NFkB pathway, and the TLR4-TRIF-IRF3 pathway. Both pathways rely on adapter proteins: MyD88, TIRAP, TRAM1, and TRIF. Each of them contains TIR domains that enable them to interact with TLR4 and with one another.

The MyD88-dependent pathway initiates at the cell membrane (**Figure 2**), while the TRIF-dependent pathway starts after TLR4 is internalized into endosomes (a process that is facilitated by CD14). In the MyD88 pathway, TIRAP first binds to the TIR domains of TLR4, subsequently recruiting MyD88. MyD88 then associates with IRAK2 and IRAK4, forming a complex known as the myddosome in a 6:4:4 ratio. This complex activates IRAK4, which leads to the recruitment of TRAF6, undergoing polyubiquitination. TRAF6 activates TAK1 and the IKK complex, resulting in the degradation of IκB and the release of NFkB. Together with MAP kinases, this cascade promotes the production of proinflammatory cytokines such as IL-1β, TNF-α, and IL-6.

In contrast, the TRIF pathway is initiated when TRAM1 binds to TLR4's TIR domain to recruit TRIF. The activation and phosphorylation of TRIF facilitate the activation of IRF3, which then translocate to the nucleus to initiate the transcription of the IFN-β gene. This pathway is crucial for antiviral and interferon responses. (Nikolay N. Kuzmich, 2017)

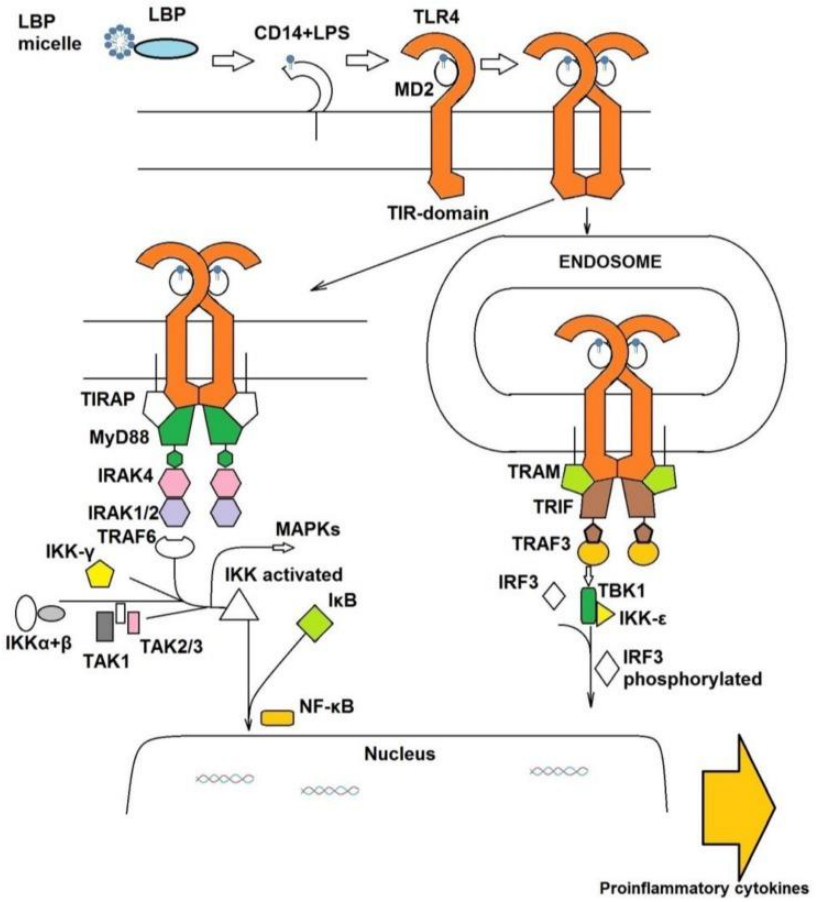

Figure 2 TLR4 Pathways *(Nikolay N. Kuzmich, 2017)*

4.2.2 Oxaliplatin as a Treatment against CRC

Oxaliplatin (**Figure 3**) is a platinum-based chemotherapeutic drug mainly used in the treatment of colorectal cancer. It belongs to the same family as cisplatin and carboplatin but it differs in its chemical structure and some aspects of its activity. After administration, oxaliplatin enters the cancer cell, where it becomes activated through the loss of its oxalate group. This process generates reactive platinum complexes capable of binding to DNA. The activated platinum compound forms covalent bonds with the nitrogen atoms of guanine and adenine bases in DNA.
This leads to a crosslinking between adjacent bases on the same DNA strand, and interstrand crosslinks between complementary strands. These crosslinks distort the DNA structure, preventing proper DNA replication and transcription.

As a result of these DNA lesions, the cell can no longer replicate its genetic material correctly. DNA damage activates cell cycle arrest and triggers apoptosis if repair mechanisms fail.

Compared to cisplatin: Oxaliplatin induces different DNA adducts that alter the three-dimensional shape of DNA more strongly. Tumor cells that are resistant to cisplatin often remain sensitive to oxaliplatin. Its action also involves oxidative stress and immune system modulation, beyond direct DNA damage. (Alexandra Fauvre, 2025)

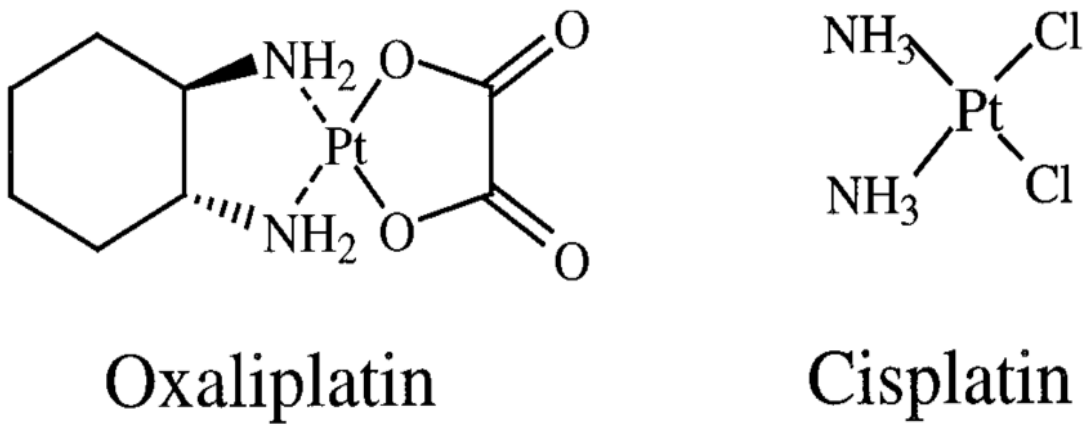

Figure 3 Structure of Oxaliplatin and Cisplatin *(J. M. Woynarowski, 2000)*

4.2.2.1 The Interaction of Oxaliplatin with the Immune system

As already mentioned above the main working mechanism of oxaliplatin is the induction of programmed cell death. However, during this process DAMPs are released which cause inflammatory actions in the long run. Tumor-derived DAMPs have the ability to activate TLRs, such as TLR4, thereby enhancing cancer cell motility, invasion, metastasis, and resistance to chemotherapy.

In this context, the expression of drug-induced DAMPs and their influence on tumor progression represent critical parameters for assessing the efficacy of oxaliplatin. Therefore, this drug can induce the release of several DAMPs from cholangiocarcinoma cells, including members of the HSP family, S100 proteins, calreticulin, and HMGB1 (**Figure 4**). These molecules subsequently activate signaling pathways such as Akt, ERK, and Cyclin-D1, which promote tumor cell proliferation and survival. (Worawat Songjang, 2022)

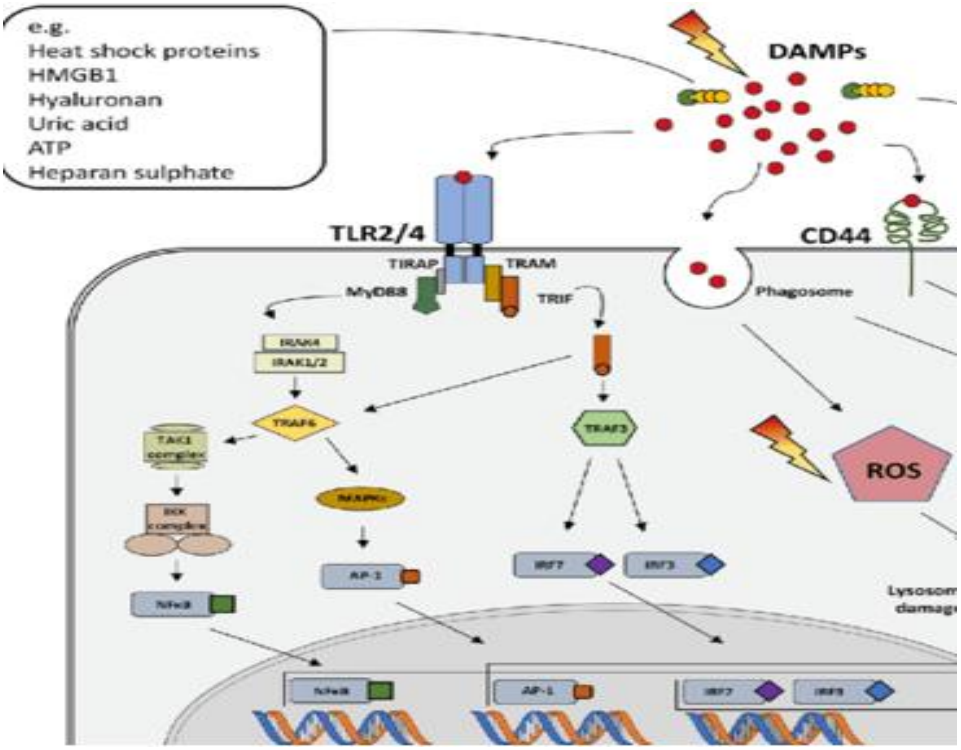

Figure 4 The Mechanism of DAMPs *(Florian Wirsdörfer, 2017)*

4.2.2.2 Effects of Oxaliplatin on TLR4

The effects of oxaliplatin on TLR4 has been a frequently researched topic. Interestingly, some studies show that oxaliplatin enhances the TLR4 pathway signaling and results in an induction of inflammation. The reason behind this phenomenon is still unknown. (Amina M. Illias, 2022) (Yoon Hee Chung, 2016) (Vanesa Stojanovska, 2018)

4.3 Types of Tumor models

4.3.1 In vitro 3D model – CT26

The most common cell cultures for in vitro screening have been 2D cell cultures as they are easily cultivated, cheap and their reproduction is very fast. However, these features miss a very important aspect – they cannot accurately replicate the characteristics of in vivo solid tumors, including their resistance to therapeutic treatments. As a result, scientists are forced to resort to in vivo tests, which again contributes to the excessive use of animals in experimental studies. (Ana S. Nunes, 2018)

Therefore, 3D cell culture models like spheroids were recently found which help solve most of the above-mentioned issues of 2D culture. One of the biggest advantages is that 3D cell cultures are able to imitate human solid tumors which are also 3D in form and therefore enables their proliferation and excessive differentiation. (Ana S. Nunes, 2018) In addition to that, spheroids were found to surpass many drug resistance mechanisms which is a very big advancement in the world of cancer science.

Structurally, spheroids consist of multiple cell layers. An important aspect is the formation of 3D multicellular tumor spheroids. Although several techniques exist, they are generally based on four main methods. All these approaches share the common principle of preventing cell attachment to surfaces, thereby promoting cell–cell interactions and enabling the cells to aggregate into spheroids. Larger spheroids typically develop a necrotic core surrounded by viable cells, including quiescent inner cells and proliferating outer cells. This organization results from limited oxygen and nutrient diffusion to the inner regions, creating gradients similar to those found in avascular tumors. These conditions lead to cell death in the core, while outer cells continue to grow and drive spheroid expansion. (Ti Ngoc Le, 2020)

For this project the CT26-Luciferase cell line was used as a 3D cell culture model. To enable non-invasive monitoring of intraperitoneal tumor growth, CT26 cells were stably transduced with firefly luciferase beforehand by retroviral transduction and selection using G418. This modification allows

longitudinal quantification of tumor burden in vivo using diffuse-light imaging tomography after systemic administration of D-luciferin. (Diana Groza, 2018)

4.3.2 In vivo Colorectal CT26 Tumor model

The CT26 cell line, derived from a BALB/c mouse, is classified as a highly aggressive (grade IV) tumor and is widely used in colorectal cancer research.

CT26 serves as a syngeneic tumor model, meaning that the tumor cells are implanted into genetically identical BALB/c mice, allowing tumors to develop in an immunocompetent system. Tumor induction can be achieved through various injection routes, such as subcutaneous, intraperitoneal, intrasplenic, intravascular, or orthotopic administration. Each method differs in technical complexity and in how closely it replicates the natural tumor environment.

Moreover, the chosen implantation route has a significant impact on metastatic spread. While subcutaneous injections rarely lead to metastasis, intraportal or intrasplenic injection commonly results in the formation of liver metastases. (Ti Ngoc Le, 2020) Interestingly it has been shown that the intraperitoneal injection of CT26 cells in the mentioned mice results in metastasis of CRC into the pancreas. (Diana Groza, 2018)

4.4 Histological analysis

4.4.1 Hematoxylin and Eosin staining

H&E staining is a broadly used staining method, used to analyze all types of tissues. It is the most reliable method in the fields of histology and pathology as it shows the microanatomy of organs, since it is very easily and fast carried out. Hence, many diseases on a daily basis can be diagnosed due to this staining method.

During the staining hematoxylin – a basic pigment – stains acidic components of cells such as the nucleus and the rough ER and through oxidation, in purple and dark blue. On the other hand, eosin – an acidic pigment – is responsible for the typical red and pinkish color of the tissues, marking the cytoplasm

proteins, smooth ER, mitochondria and collagens, which are all basic. (John K. C., 2014)

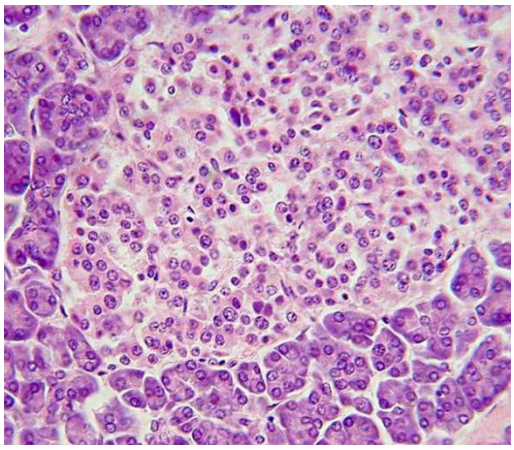

Figure 5 H&E Staining of a Pancreas
(Chandra Sekhar Singh, 2015)

4.4.2 Immunohistochemical staining (IHC)

Through the IHC-staining only specific compounds of tissue can be analyzed, that are able to bind to certain antibodies. Hence, it has been in use to assist the visualization and diagnosis of solid tumors and cytological specimens for almost 50 years now. In this method, antibodies specifically bind to target antigens and are visualized using labels, such as enzymes or fluorescent dyes, allowing detection under a microscope. Two main approaches are commonly used: direct staining, in which the primary antibody is labelled, and indirect staining, where a labelled secondary antibody is used to detect the primary antibody. (Hitoshi Ozawa, 2019)

4.4.2.1 Direct IHC staining

This method is based on an antigen-antibody interaction of the desired molecule. In this case the antibody is connected to a marker for example a chromogenic substrate. Although this is considered an easy method it is not as frequently used as indirect staining, since the intensity of its signal is often very low (**Figure 6**).

4.4.2.2 Indirect IHC staining

To improve the above-mentioned issue, indirect IHC staining was found. Indirect staining means there is not one antibody involved but two. The first antibody binds to the antigen in question while the second antibody binds to the Fc-region of the first one. This secondary antibody is also bound to a marker that is often fluorescent. This method has proven its success due to the countless secondary antibodies that can bind to primary antibodies, allowing the signal to be stronger. The only disadvantage is that it also creates much background (**Figure 6**). (Hitoshi Ozawa, 2019)

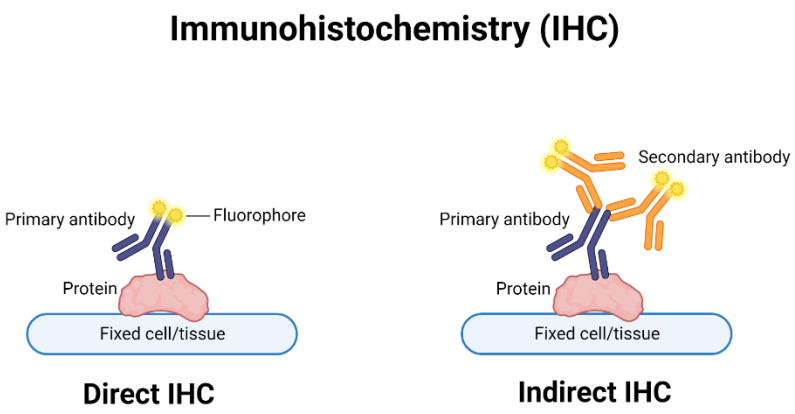

Figure 6 Direct vs Indirect IHC *(Melissa Eilbes, 2025)*

4.4.3 Horseradish Peroxidase Staining (HRP)

HRP staining is a type of IHC staining where horseradish peroxidase is used as an antibody conjugate. HRP itself is an enzyme – α-helical glycoprotein - found in the horseradish plant (**Figure 7**). A redox reaction causes the HRP to release substrates, that dye the antigen in question. This is due to the fact that HPR possesses a haem-group as well as a catalytic ferric ion within a porphyrin ring, and additionally two calcium atoms. The colored tissue usually becomes brown. HRP is not only used in IHC but also staining ELISA and western blots.

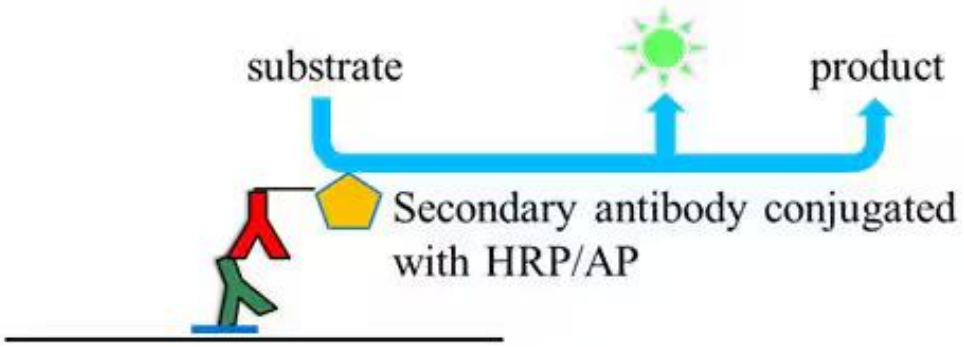

Figure 7 Mechanism of HRP staining *(Sambrook J., 1989)*

4.5 TLR4 Downstream Targets

4.5.1 MyD88

As already mentioned, the MyD88 is involved in the signaling action of the TLR pathways and also interleukin-1 receptor families. The MyD88 adapter protein was initially identified as the product of a newly discovered gene belonging to the myeloid differentiation primary response (MyD) gene family, which is induced during the differentiation of myeloid cells. In murine $M1D^{+}$ myeloleukemic cells, IL-6–induced activation of the MyD88 gene resulted in growth arrest and differentiation, suggesting that MyD88 plays a role as a mediator of terminal myeloid differentiation.

In 1994, sequence analysis revealed a homology between the C-terminal region of MyD88 and the TIR domains present in members of the Toll and interleukin-1 receptor families. Unlike other TIR-containing proteins, MyD88 is a purely cytoplasmic protein that also possesses an N-terminal death domain.

Furthermore, MyD88 mRNA was later detected in a wide range of adult human tissues, not only in myeloid cells. Eventually, human MyD88 was characterized as an adaptor molecule in both Toll-like receptor and interleukin-1 receptor signaling pathways. Through its C-terminal TIR domain, MyD88 receives activation signals from these receptors and, via its N-terminal death domain, initiates downstream signaling cascades. (Clauberg Sigrid, 2011)

4.5.2 TRAM1

TRAM1, also known as TICAM2, is a key adapter protein involved in TLR4 signaling. It belongs to the family of TIR-domain-containing adapter proteins, which includes MyD88, TIRAP, TRIF, and TRAM1. These adapter proteins are essential for transmitting signals from TLRs, allowing the recognition of pathogens or DAMPs to elicit appropriate cellular responses. (Luke A. J. O'Neill, 2003)

TRAM1 plays a central role in the TRIF-dependent branch of TLR4 signaling. While TLR4 can initiate signaling through the MyD88-dependent pathway at the plasma membrane leading to early NFkB activation and proinflammatory cytokine production, TRAM1 mediates signaling from endosomal TLR4 to recruit TRIF. This interaction is critical for the activation of downstream pathways, including the phosphorylation of IRF3, which drives type I interferon production, and the delayed activation of NFkB, contributing to the late-phase inflammatory response.

Structurally, TRAM1 contains a TIR domain, which enables its interaction with TLR4, but lacks a death domain, distinguishing it from MyD88. The protein is also N-terminally myristoylated, which facilitates its association with cellular membranes—an essential feature for its function in endosomal signaling.

Overall, TRAM1 serves as a pivotal adapter that specifically mediates TRIF-dependent TLR4 signaling, thereby regulating antiviral and immunomodulatory responses, while MyD88 primarily controls the early proinflammatory signaling events. (Luke A. J. O'Neill, 2003)

4.5.3 NFkB

NFkB is a specific transcription factor that regulates immune responses, cell proliferation, and apoptosis. The structure of NFkB is built by five to seven protein subunits that are organized around a domain of 300 amino acids. Two subunits usually associate to form a functional dimer. There are five main NFkB subunits known to this point:

- NFkB1 (p50 or its precursor p105)
- NFkB2 (p52 or its precursor p100)
- RelA (p65)
- RelB
- c-Rel

This transcription factor primarily binds to the κB recognition motif within human DNA. During an active immune response, this binding stimulates the transcription of cytokines and adhesion molecules, which are essential for immune regulation and signaling. The activation of NFkB is induced mainly by tumor necrosis factor alpha and interleukin-1 as part of the immune response. (Lucas G. A. Ferreira, 2022)

NFkB is present in nearly all human cells in two different forms. Firstly, there is the inactive form of NFkB, that is bound to IkB in the cytoplasm. Secondly there is the active form which can be found in the nucleolus. Therefore, in antibody producing cells, such as b-cells, t-cells, and macrophages, NFkB is always in its active form. (Jäger Doreen, 2014)

The activation of NFkB is depending on numerous factors, for example physical stress, chemicals, signaling molecules, and most importantly cytokines and growth factors. Once the activation is done, there are two different pathways that transmit the signal. Either the classical canonical pathway or the alternative non-canonical pathway. To start the process of signaling in both pathways, the IKK needs to be activated in order to phosphorylase the IkB bound to the NFkB. Afterwards active NFkB translocate to the cell nucleus to initiate the gene expression. The expression results in activation of the immune system and proliferation of proinflammatory molecules. (Lucas G. A. Ferreira, 2022)

4.6 HIF1-α in Cancer

HIF-1 is a transcription factor that is released in cells in case of hypoxia. Hypoxia is a state in which cells suffer from a low partial pressure of inspired

oxygen. This phenomenon usually occurs in tumor cells. As a result, cells have to provide themselves with transcription genes which excessively increase the glucose metabolism, angiogenesis, iron metabolism, and the cell cycle. This is when HIF-1s play a very big role, as they are oxygen sensitive transcription factors that accumulate during hypoxia, activate HIF-1 specific genes and with that ensure the adaptation to the low oxygen levels in the tumor cells.

The HIF-1 is a heterodimer built by its subunits HIF-1α and HIF-1β. HIF-1α also possesses over a so-called oxygen-depending degradation domain, which ensures its stability. In order to bind on the DNA and process proliferating molecules, HIF-1 must bind the HRE that is located near the DNA-promotors. (Franziska Beuing, 2022)

4.6.1.1 Crosslink between TLR4 and Overexpression of HIF-1α

Not only is the TLR4 involved in proliferation of cancer cells, but recent studies have shown that there is a crosslink between it and HIF-1α, causing the transcription factor to be overexpressed. This crosslink has been proven to cause poor diagnosis in different forms of cancer. (Xiao YANG, 2018) (Shengwei Han, 2016) (Ping Fan a, 2012)

The reason behind this is still being researched, but it has been proved in numerous studies that ligand LPS of TLR4 increases the expression of HIF-1α by some studies. (Shengwei Han, 2016) Keeping this in mind, these findings may also occur for colon cancer cells, which is the main focus of this thesis.

5 Aim of the study

The aim of this project was to investigate the effects of oxaliplatin on the TLR4-pathway in CT26 Luc tumor bearing mice and CT26luc tumor spheroids by immunohistochemical means.

In particular, the study focused on key downstream signaling components, including NFkB, TRAM1, and MyD88, which are known to play central roles in inflammation and tumor progression. In addition to assessing the effects of oxaliplatin treatment, an important objective was to characterize the baseline expression and localization of these targets in healthy tissue, tumor regions, and transition zones in untreated mice, and subsequently compare these patterns to those observed under oxaliplatin treatment.

To achieve this, an in vivo mouse model using CT26 tumor cells and an in vitro 3D spheroid model were employed to mimic physiological tumor conditions. Through histological and immunohistochemical analysis, the expression and distribution of these proteins were evaluated. The overarching goal was to determine whether oxaliplatin modulates TLR4-mediated signaling and how its effects relate to the spatial expression patterns of these markers within different tissue regions.

6 Materials and Methods

6.1 Sections

For the sections a cryostat (SLEE CRYOSTAT MNT) was used. The organs – embedded in Tissue Tek® - were cut in a thickness of 6µm, and the sectioning was performed at a temperature between -20°C and -18°C. The cut tissues were put on glass slides and stored at -80°C.

6.2 H&E Staining

Frozen tissue slides were removed from the freezer, placed on a paper towel, and the organs of interest were encircled using a histological pen (Elite PAPA Pen, Cedarlane Labs). The marked areas were immediately fixed in 4% paraformaldehyde for 7 minutes by gently pipetting the fixative into the circled region, avoiding direct contact with the tissue. Following fixation, the PFA was discarded, and excess liquid was removed by tapping the slide edge on a paper towel.

Slides were rinsed twice in phosphate-buffered saline (PBS; Sigma Life Science) for 3 minutes each to remove residual embedding compound. Afterwards, they were washed under a gentle stream of tap water for 1 minute. The staining was performed in Mayer's hematoxylin for 2 minutes, followed by rinsing in tap water for 20 seconds to allow bluing of the nuclei due to increasing pH. The slides were then immersed in NH_4OH for 20 seconds and rinsed again in tap water for 1 minute.

Afterward, slides were stained in eosin for 20 seconds to visualize acidophilic cytoplasmic structures in varying shades of red, followed by a 10-second rinse in running tap water. Staining intensity may vary between tissues, and minor adjustments to incubation times were made when necessary. Tap water was avoided if chlorinated, as it can interfere with staining quality.

Dehydration was carried out by briefly immersing slides (1 second each) in an ascending ethanol series (3×70%, 3×96%, 3×100%). The slides were then cleared in two successive xylene baths for 1 minute each to remove residual alcohol.

Finally, the stained sections were mounted with Entellan® (Merck) for long-term preservation and microscopic analysis.

All the sections derived from mice used in this project were stained first with H&E to provide an overview of the mouse tissues.

6.3 IHC Staining of mouse sections

For this project, indirect IHC staining was used. The fixation of the tissues was performed as mentioned above in the H&E section. After the fixation, each mouse section was then covered with 100 µL of blocking buffer (SmartBlock™) and incubated for 1 hour at room temperature in the dark to minimize light exposure.

Following the blocking step, 100 µL of either the primary antibody or the corresponding isotype control antibody was applied to each tissue section. The slides were incubated for 2 hours at room temperature or alternatively overnight at 4 °C. After incubation, excess antibody was removed by washing the slides three times with PBS for 3 minutes per wash.

A secondary antibody was subsequently added to the sections and incubated for 2 hours at room temperature in the dark. This step was followed by three additional PBS washes of 3 minutes each. Nuclear and membrane counterstaining was performed using a DAPI/WGA solution for 30 minutes. All handling of DAPI was carried out while wearing nitrile gloves to ensure safe laboratory practice.

In the final steps, slides were washed twice with PBS for 3 minutes, then mounted with approximately 10 µL of Vectashield® mounting medium per section. Coverslip edges were sealed with nail polish to prevent drying and

photobleaching. Prepared slides were stored in the dark until microscopic analysis.

6.3.1 Used Antibodies and staining method of mouse sections

All the sections were stained against the TLR4 using 3 different types of prim. AB to visualize the TLR4 pathway, which are NFkB (NF-κB p65 Polyclonal antibody; proteintech), TRAM1 (TRAM1 Polyclonal antibody; proteintech) and MyD88 (MYD88 Polyclonal antibody; proteintech). As for the counterstain a sec. AB was used – the Nano Sec AB Alexa Flour® 568 (ChromoTek Nano-Secondary® anti-human IgG/anti-rabbit IgG, recombinant VHH, Alexa Fluor® 568; proteintech). In order to compare the antibody signals to a control AB, an isotype control AB-mix (Rabbit IgG Isotype Control; ThermoFisher) was used. The exact solutions and concentrations of the prim. and sec. ABs are documented in the solutions section 6.7.2.

From each mouse 4 slides in total were derived, and 2 sections were put on each slide. One slide was used to perform an H&E staining on (**Figure 8**), 2 slides were used for the IHC-staining and one slide was kept unstained as an extra in the -80°C freezer. The IHC-stained sections of each mouse were organized as follows: One slide is divided in two sections. The first section was prepared using the isotype control AB-mix. The second section was prepared with NFkB as a prim (**Figure 8**). AB. As for the second slide of the IHC-staining (also here two sections on one slide **Figure 8**) the first section was stained against TRAM1 prim. AB and the second section against MyD88 (**Figure 8**). The counterstaining with the sec. AB (ChromoTek Nano-Secondary® anti-human IgG/anti-rabbit IgG, recombinant VHH, Alexa Fluor® 568) was performed on all the sections of the IHC-staining. Additionally, all the sections were prepared with a DAPI-solution to visualize the cell-nuclei.

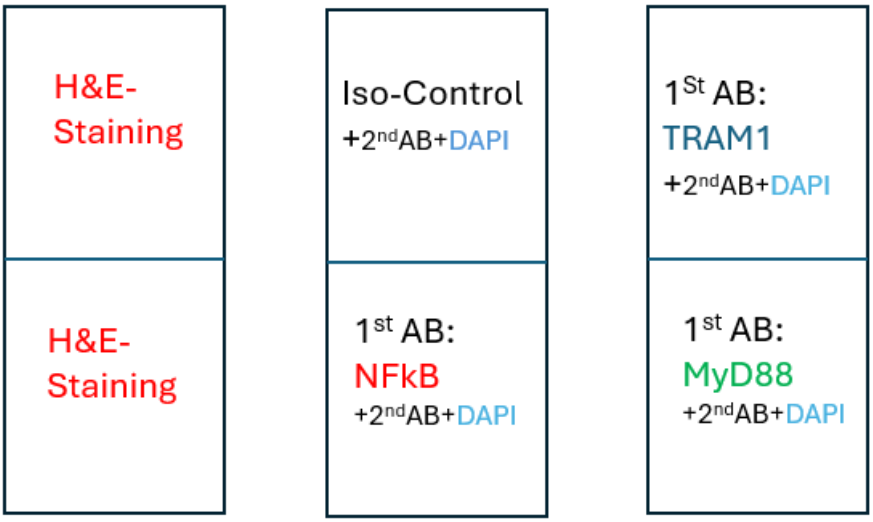

***Figure 8 IHC-Staining of all mouse sections**. IHC-Staining Method of Mouse Sections. For each mouse one slide was H&E-stained, the second slide was stained for an Iso-Control and NFkB the third slide was stained for TRAM1 and MyD88.*

6.3.2 Information on the mice used in the project

In total 4 different mice were used for this project: MCT1147, MCT0969, MCT1171 and MCT0957. Each mouse was injected intraperitoneally with1*10^5 CT26-Luc cells on day 0 of the in vivo experiment. Only 2 of the above-mentioned mice were treated with oxaliplatin, which were MCT1147 and MCT0969. The treatment took place on the third and sixth day of their trial with exactly 6mg/kg oxaliplatin. After their euthanization (MCT1147 on day 24, MCT1171 on day 24, MCT0969 on day 22, MCT0957 on day 23) only the pancreas was used for the staining process, as the CT26 carcinoma cells metastasize in that region. The pancreatic tissue was cut and differentiated in pancreas tissue with CT26 tumor nodules and just CT26 tumor nodules without pancreas. After that the tissues were embedded in Tissue Tek®.

All the derived tissues, either pancreas tissue with tumor nodules or just tumor nodules were sectioned and stained with the above-mentioned methods and same prim. and sec. ABs.

Mouse ID	Treatment	Pancreas Sections	Tumor Sections	Thickness (µm)
MCT1147	oxaliplatin 6 mg/kg	4 slides	4 slides	6
MCT0969	oxaliplatin 6 mg/kg	4 slides	4 slides	6
MCT1171	untreated	4 slides	4 slides	6
MCT0957	untreated	4 slides	4 slides	6

Table 1 Overview of the mice involved.

6.4 IHC Staining of the spheroid sections

The staining process of the spheroids was conducted in the same way as the mouse tissues, using the same prim., sec. ABs, iso-control AB-mix and DAPI - solutions. Only some adjustments were made in the protocol to fit the spheroids, since the tissues are more fragile and smaller. The fixation process was the exact same, but the staining procedure was adjusted by reducing the volume put on the sections of each solution from 100 µL to 50 µL.

From each spheroid one slide was derived and approximately 12 spheroid sections were positioned on that slide (**Figure 9**). The spheroids were arranged in a total of 4 rows and 3 columns. The first row was prepared with the iso-control AB-mix (Rabbit IgG Isotype Control; ThermoFisher) (**Figure 9**) the second row with NFkB (**Figure 9**) (NF-κB p65 Polyclonal antibody; proteintech; proteintech), the third row with TRAM1 (**Figure 9**) (TRAM1 Polyclonal antibody; proteintech) and the fourth row with MyD88 (**Figure 9**) (MYD88 Polyclonal antibody; proteintech). All the sections were counterstained with the Nano Sec AB Alexa Flour® 568 (ChromoTek Nano-Secondary® anti-human IgG/anti-rabbit IgG, recombinant VHH, Alexa Fluor® 568; proteintech).

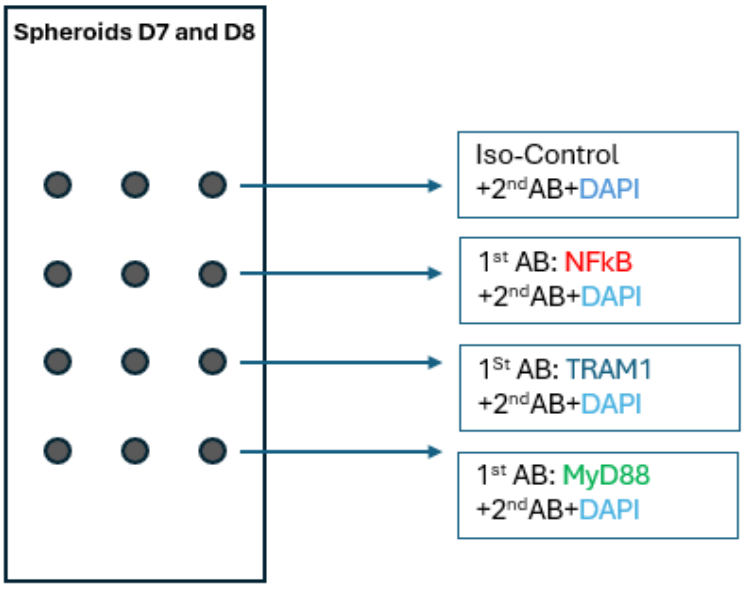

***Figure 9 IHC-Staining of spheroid sections**. The first row was a control, the second was stained for NFkB, the third for TRAM1 and the last for MyD88.*

6.4.1 CT26 Luc spheroids

The spheroids were cultivated as well as harvested and embedded in Tissue Tek® by my supervisor. In total 6 spheroids were sectioned, which were harvested on day 7 and on day 8 after cultivation and 3 different treatments from each harvesting day were differentiated. One spheroid of each harvesting day was left untreated as a control; one was treated with 25 µM oxaliplatin and one with 100 µM.

Spheroid	Harvest Day	Treatment	Slides	Section Thickness (µm)
Spheroid 1	Day 7	Untreated	1	6
Spheroid 2	Day 7	25 µM oxaliplatin	1	6
Spheroid 3	Day 7	100 µM oxaliplatin	1	6
Spheroid 4	Day 8	Untreated	1	6
Spheroid 5	Day 8	25 µM oxaliplatin	1	6
Spheroid 6	Day 8	100 µM oxaliplatin	1	6

Table 2 Spheroid overview.

6.5 HRP Staining of mouse tissue and tumor sections

The fixation steps are similar to the fixation steps in again the H&E staining.

Afterwards, frozen tissue sections were first rinsed in PBS containing 0.025 % Triton X-100 for 5 minutes to remove any remaining embedding medium and to permeabilize the cell membranes. Slides were then briefly washed in PBS for 1 minute and transferred to a humid chamber prepared with paper towels.

Each tissue section was covered with two drops of blocking buffer (horse serum provided by the staining kit: ImmPRESS® HRP Horse Anti-Rabbit IgG PLUS Polymer Kit) and incubated for 45 minutes at room temperature to reduce nonspecific binding. The blocking solution was then removed, and 100 µL of primary antibody HIF1α (HIF1A Polyclonal Antibody; ThermoFisher) or the corresponding isotype control (Rabbit IgG Isotype Control; ThermoFisher) antibody was applied to each section. Incubation was carried out for 2 hours at room temperature or alternatively overnight at 4 °C.

After incubation, the slides were washed twice with PBS for 3 minutes each. Endogenous peroxidase activity was blocked by applying two drops of BLOXALL® (also from the same kit ImmPRESS® HRP Horse Anti-Rabbit IgG PLUS Polymer Kit) solution to each section for 10 minutes, followed by two additional PBS washes of 3 minutes.

Next, two drops of the HRP-conjugated secondary antibody (provided with the kit) were applied to each section and incubated for 30 minutes at room temperature. Slides were then washed three times in PBS for 2 minutes per wash. During this step, the DAB substrate was freshly prepared by mixing equal volumes of solutions 1 and 2. Approximately 100 µL of the prepared DAB solution was applied to each section and allowed to develop until optimal staining intensity was reached. When using a new primary antibody for the first time, staining development was monitored microscopically to determine the appropriate incubation time.

To complete the staining, slides were washed twice with distilled water for 2 minutes, counterstained with hematoxylin for 1.5 minutes, and then rinsed twice again in water for 2 minutes. Finally, sections were dehydrated through an ascending ethanol series, cleared in xylene, and mounted using Entellan® mounting medium for long-term preservation and brightfield microscopy.

The HRP staining was performed on the mouse sections mentioned in **table 1**. In this case only 2 slides were derived from each tissue, the pancreas tissue with CT26 tumor nodules as well as the CT26 tumor nodules without pancreas. One of each slide was used for the staining and the other was again kept as an extra in the -80°C freezer. On the stained slides two sections were positioned again the first section was prepared with an iso-mix AB corresponding to the HIF1α (**Figure 10**). The second section was as prepared with the HIF1α as a prim. AB. To both sections the sec. AB provided in the kit was added.

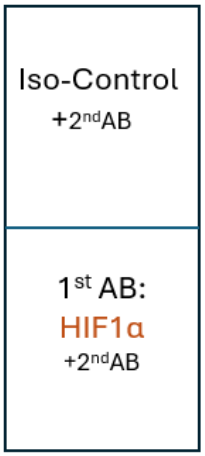

Figure 10 HRP-Staining of mouse sections.

6.6 Microscopy of the Stained Sections

The results of both the H&E-staining and HRP-staining were analyzed with a light microscope (Olympus BX53 light microscope) in bright field mode. Captured images were acquired at multiple magnification levels using an Olympus DP-73 color camera, with image acquisition and processing carried out via sellSens Standard software provided by Olympus Corporation. The pictures taken were in magnification 20x and from each mouse tissue a whole scan (20x) of the tissue was additionally made.

Objective	Magnification
2x	Plapon2X/0.08 Apo
4x	UPLSAPO4X/0.16 U Plan S Apo
10x	UPLSAPO10X2/0.40 U Plan S Apo
20x	UPLSAPO20X/0.75 U Plan S Apo
40x	UPLSAPO40X2/0.95 U Plan S Apo

Table 3 Magnifications of the light microscope.

As for the IHC-staining, a fluorescence microscope (Olympus IX73 inverted microscope) was used, to visualize the mouse and spheroid sections. The pictures were taken in 2 different magnifications, 20x and 60x using the Olympus XM10 digital microscope camera with the cellSens Standard software from Olympus again.

Objective	Magnification
10x	UPLFLN10X2/0.30
10x	CPLN10XPH/0.25
20x	LCACH20XPH/0.45
40x	UPLSAPO40X2/0.95
60x	PLAPON60XO/0.42

Table 4 Magnifications of the fluorescence microscope.

Image acquisition was performed using different imaging modes depending on the fluorophores applied, including phase contrast as well as fluorescence channels for Cy3 and DAPI. For each staining cycle, exposure settings were individually optimized for every combination of filter and objective. The corresponding exposure times used for analysis are summarized in the following tables.

20x Magnification of the mouse project			
Filter	**Exposure Time (ms)**	**Gain**	**Scale**
PH	-	8.1	0-16383
CY3	500	8.1	0-16383
DAPI	500	8.1	0-16383

Table 5 Fluorescence settings for the mouse project (20x magnification).

60x Magnification of the mouse project			
Filter	**Exposure Time (ms)**	**Gain**	**Scale**
PH	-	20	0-16383
CY3	50	20	0-16383
DAPI	50	20	0-16383

Table 6 Fluorescence settings for the mouse project (60x magnification).

20x Magnification of the spheroid project			
Filter	**Exposure Time (ms)**	**Gain**	**Scale**
PH	-	0	0-16383
CY3	400	0	0-16383
DAPI	400	0	0-16383

Table 7 Fluorescence settings for the spheroid project (20x magnification).

60x Magnification of the spheroid project			
Filter	**Exposure Time (ms)**	**Gain**	**Scale**
PH	-	0	0-16383
CY3	40	0	0-16383
DAPI	40	0	0-16383

Table 8 Fluorescence settings for the spheroid project (60x magnification).

6.7 Solutions

The following tables provide an overview of the solutions used for H&E-, IHC- and HRP- staining.

6.7.1 Solutions for the H&E-Staining

Solutions	Components	Amount
PFA 4%	HEPES 20 mM	19.056 g for 4 L
	NaCl 150 mM	35.064 g for 4 L
	MiliQ-Water	ad 4 L
	NaOH for adjusting pH to 7.4	-
	4 % Paraformaldehyde	160 g for 4 L
Ammonium- Water	Aqua dest.	250 mL
	Ammonium solution 32 %	10 drops
Hematoxylin-solution	Harris Hematoxylin solution	160 mL
	Aqua dest.	80 mL
Eosin- solution	Eosin Y solution	25 mL
	Aqua dest.	200 mL
	Acetic Acid glacial	0.125 mL

Table 9 Solutions for the H&E-staining.

6.7.2 Solutions for the IHC-Staining

Solutions	Components	Amount
DAPI (1:2000) & WGA 1:1000 Mix	WGA (Rhodamine Wheat Germ Agglutinin 1 mg/mL)	2 µL
	DAPI (DAPI Staining Solution 1 mg/mlL	1 µL
	PBS (Dulbecco's Phosphate Buffered Saline)	1997 µL
Prim. AB-Mix (1:100)	NF-κB p65 Polyclonal antibody	5 µL
	SmartBlock™ 10 mL	495 µL
Prim. AB-Mix (1:100)	TRAM1 Polyclonal antibody	5 µL
	SmartBlock™ 10 mL	495 µL
Prim. AB-Mix (1:400)	MYD88 Polyclonal antibody	1.25 µL
	SmartBlock™ 10 mL	498.75 µL
Sec. AB-Mix (1:1000)	ChromoTek Nano-Secondary® anti-human IgG/anti-rabbit IgG	1 µL
	SmartBlock™ 10 mL	999 µL
IsoC-Mix (1:999)	Rabbit IgG Isotype Control	1 µL
	SmartBlock™ 10 mL	999 µL

Table 10 Solutions for the IHC-staining.

6.7.3 Solutions for the HRP-Staining

Solutions	Components	Amount
PFA 4%	HEPES 20 mM	19.056 g for 4 L
	NaCl 150 mM	35.064 g for 4 L
	MiliQ-Water	ad 4 L
	NaOH for adjusting pH to 7.4	-
	4 % Paraformaldehyde	160 g for 4 L
Ammonium- Water	Aqua dest.	250 mL
	Ammonium solution 32 %	10 drops

Hematoxylin-solution	Harris Hematoxylin solution	160 mL
	Aqua dest.	80 mL
Prim. AB-Mix (1:200)	HIF1A Polyclonal Antibody	2.5 µL
	SmartBlock™ 10 mL	497.5 µL
IsoC-Mix (1:999)	Rabbit IgG Isotype Control	1 µL
	SmartBlock™ 10 mL	999 µL

Table 11 Solutions for the HRP-staining.

6.8 Reagents and Product Information

- Acetic acid glacial (VWR® Prod. 20104.334, Batch 14A160513)
- Ammonium hydroxide solution (Sigma- Aldrich®, Prod. 221228 LOT # SZBD3180V)
- DAPI Staining Solution 1 mg/ml (Lot no. 5200903062, Prod. 130-111-570, Prod. 107961)
- Entellan® new, rapid mounting medium (Merck, LOT HX42534561)
- Eosin Y solution (Sigma- Aldrich®, LOT # MKBQ9365V, Prod. 318906)
- Ethanol denatured ≥ 99,8% with appr. 1% MEK (Carl Roth®, Cas- Nr. [64-17-5] EG- Nr. 200-578-6, UN- Nr. 1170, item number K928.22)
- Harris Hematoxylin solution (Carl Roth, Art. Nr. X903.3)
- HEPES (Lot. no 7IO15011)
- ImmPRESS® HRP Horse Anti-Rabbit IgG PLUS Polymer Kit (LOT: ZK0225; REF: MP-7801)
- PBS: Dulbecco's Phosphate Buffered Saline (Sigma Life Science Lotno. RNBH3161, Prod. D8537)
- PFA 4% in HBS pH 7,4 (#280220)
- Rhodamine Wheat Germ Agglutinin 1 mg/ml (Vector Lab Inc. Lot no. ZD0510, Prod. RL-1022)
- SmartBlock™ 10 ml (Lot no. 113010, Prod. 113 500)
- Tissue-Tek® (Lot no.1134700024, Prod. 4583)

- VECTASHIELD® Antifade Mounting Medium (Lot no. ZF0409, Prod. H-1000

6.9 Materials and Product Information

- Coverslips Carlroth 24x50 mm (Art. Nr. 1871)
- Elite PAP Pen (CLSG80125)
- Menzel-Gläser Superfrost® Plus Microscope Slides (REF J1800AMNZ)

6.10 Antibodies and Product Information

- ChromoTek Nano-Secondary® anti-human IgG/anti-rabbit IgG, recombinant VHH, Alexa Fluor® 568 (Proteintech Lot no: 201252-02; srbAF568-1)
- HIF1A Polyclonal Antibody (ThermoFisher- PA1-16601)
- Isotype Control (Rabbit IgG Isotype Control – Cat.No. 02-6102; ThermoFisher)
- MyD88 (MYD88 Polyclonal antibody (Proteintech; 29946-1-AP)
- NF-κB p65 Polyclonal antibody (Proteintech; **Cat No.** 10745-1-AP)
- TRAM1 (TRAM1 Polyclonal antibody (Proteintech; **Cat No.** 12705-1-AP)

6.11 Devices and Product Information

- cellSens Standard Olympus (Shinjuku, Tokyo, Japan)
- Olympus BX53 light microscope Olympus (Shinjuku, Tokyo, Japan)
- Olympus DP-73 color camera Olympus (Shinjuku, Tokyo, Japan)
- SLEE CRYOSTAT MNT (Slee medical GmBH, Mainz, Germany)

6.12 Declaration on the Use of AI-Assisted Tools

During the preparation of this master's thesis the translation tool DeepL (https://www.deepl.com/de/translator) was used to support the translation of certain passages from German into English whenever my own language proficiency was not sufficient to ensure accurate and fluent wording.

In addition, ChatGPT (https://openai.com/de-DE/) was occasionally consulted for non-scientific support tasks, including suggestions regarding formatting, layout decisions, and the placement or integration of figures and images. In a limited number of cases, ChatGPT was also used to obtain recommendations for improving the clarity and readability of the language.

No confidential or sensitive research data was entered into or processed by these tools. Furthermore, AI-based tools were not used to create scientific ideas, formulate hypotheses, generate research results, perform analyses, or derive interpretations and conclusions. All outputs and suggestions provided by these tools were critically evaluated, revised where necessary, and independently verified by the author before being incorporated into this thesis.

7 Results & Discussion

7.1 Results of the IHC-Staining in CT26 Colorectal Tumor Model

7.1.1 H&E-Staining of Pancreas and Tumor Nodules

As for the mouse tissues used, H&E-staining was firstly performed to provide an overview of the whole organs of the tumor nodules and the healthy pancreas tissues. The following pictures (**Figure 11** and **Figure 12**) show the described tissues taken with the 10x magnification.

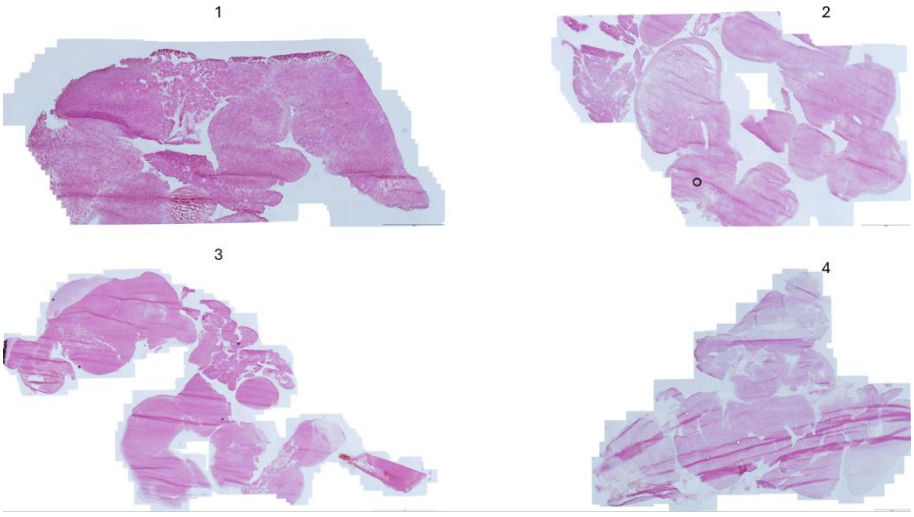

Figure 11 Bright field microscopy images of H&E-stained pancreas sections in 10x magnification *(scale bar: 2 mm)**.** The sections provide an overview of MCT1147 (1), MCT0969 (2) which were treated with oxaliplatin and MCT1171 (3) and MCT0957 (4) which did not receive a treatment.*

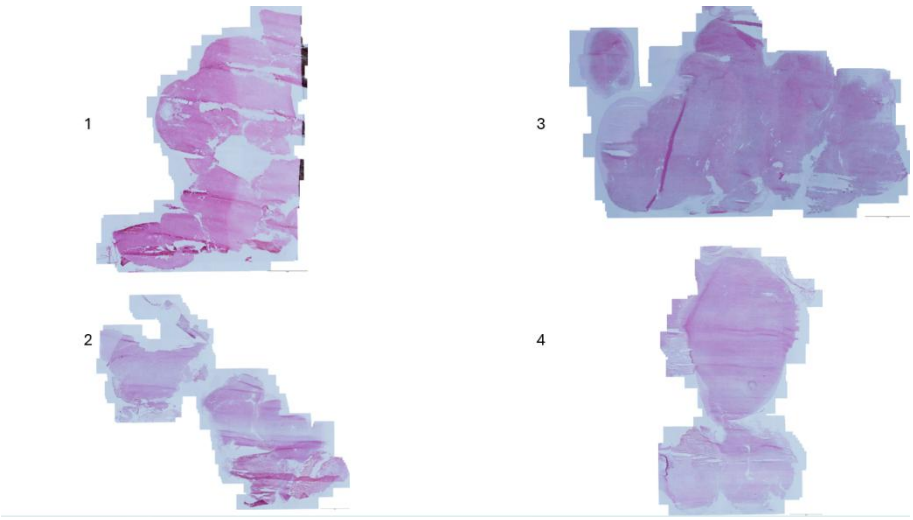

Figure 12 Bright field microscopy images of H&E-stained tumor sections in 10x magnification *(scale bar: 2 mm)**.** The sections provide an overview of MCT1147 (1), MCT0969 (2) which were treated with oxaliplatin and MCT1171 (3) and MCT0957 (4) which did not receive a treatment.*

7.1.2 NFkB-Expression in Pancreatic Tissue

As already mentioned, for each mouse Iso-Ctrl staining was done in the process to make sure that the antibodies used show specific binding and to prevent background-staining. The following figures (**Figure 13-Figure 14**) present images of isotype controls from pancreatic tissue of the mice used in the experiment, taken in 20x magnification.

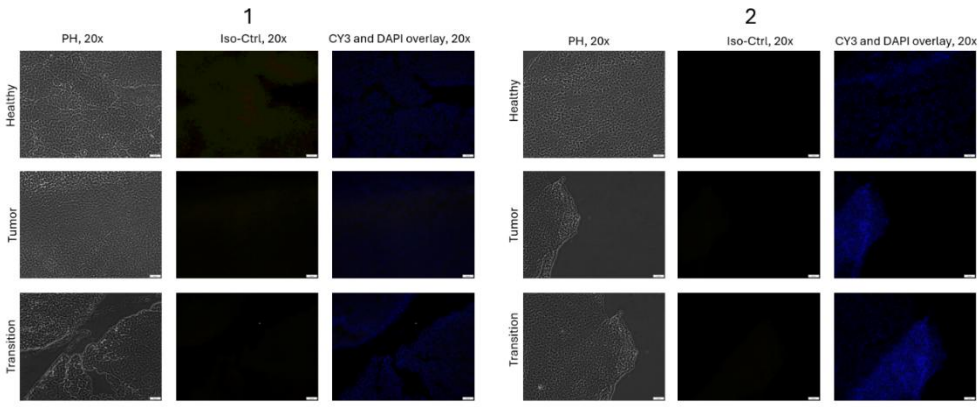

***Figure 13 Iso-Ctrl for the pancreatic tissue for MCT1147(1) and MCT0969 (2) that were treated with oxaliplatin**. Pictures were taken in 20x (scale bar: 50 µm) magnification and also differentiated in healthy-, tumor- and transition-tissue. No specific expression e.g. yellow spots are visible in the CY3 filter. Only the blue color of the cell nuclei from the DAPI-staining is visible in the CY3+DAPI overlay both 20x and 60x.*

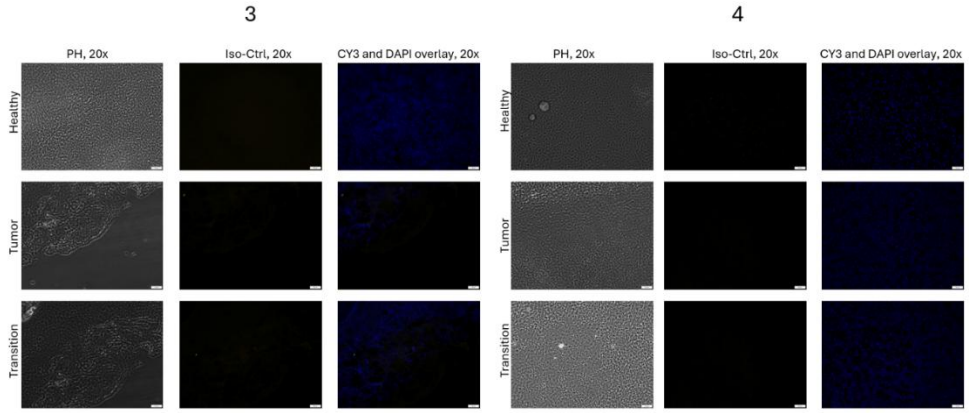

***Figure 14 Iso-Ctrl for the pancreatic tissue for MCT1171(1) and MCT0957(2) that were treated with oxaliplatin** Pictures were taken in 20x (scale bar: 50 µm) magnification and also differentiated in healthy-, tumor- and transition-tissue. No specific expression e.g. yellow spots are visible in the CY3 filter. Only the blue color of the cell nuclei from the DAPI-staining is visible in the CY3+DAPI overlay both 20x and 60x.*

Analysis of NFkB signaling demonstrates that the expression of this transcription factor is highly dependent on the type of tissue examined. Specifically, it is evident that signal intensity is higher in healthy tissue areas as well as in the transitional zones between healthy and tumor tissue, compared to the tumor regions themselves. These differences are particularly apparent in **Figure 15**, **Figure 16** and **Figure 18**. The increased expression in non-tumor regions suggests that NFkB is active or at least present in a preparatory form in these areas, whereas the tumor tissue exhibits significantly reduced signal intensity.

Furthermore, it is notable that the localization of the NFkB signal within cells is not distinctly nuclear, as would be expected for fully activated NFkB complexes. Instead, a more subcellular distribution is observed, which is especially visible in the 60x magnification images in **Figure 15, Figure 16** and **Figure 18**. This subcellular localization could have several explanations. On the one hand, it might reflect limited signal quality or intensity, possibly due to technical constraints in immunofluorescence staining or signal amplification. On the other hand, it could indicate that NFkB is not fully activated under the given condition. The observed subcellular distribution suggests that the transcription factor may be only partially activated or remain in the cytoplasm.

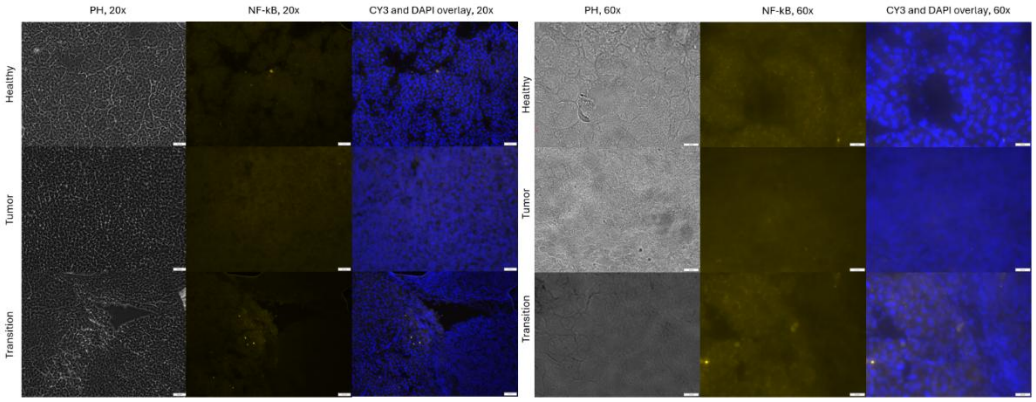

Figure 15 NFkB-Expression in MCT1147 treated with oxaliplatin*. Pictures were taken in 20x (scale bar: 50 µm) and 60x (scale bar: 20 µm) magnification and differentiated in healthy-, tumor- and transition-tissue. There is some expression visible in form of yellow punctate spots and diffuse yellow staining in pancreatic and transitional cells in the Cy3 and CY3+DAPI overlay filter especially in the 60x magnification. The blue color of the cell nuclei from the DAPI-staining is visible in the CY3+DAPI overlay both 20x and 60x.*

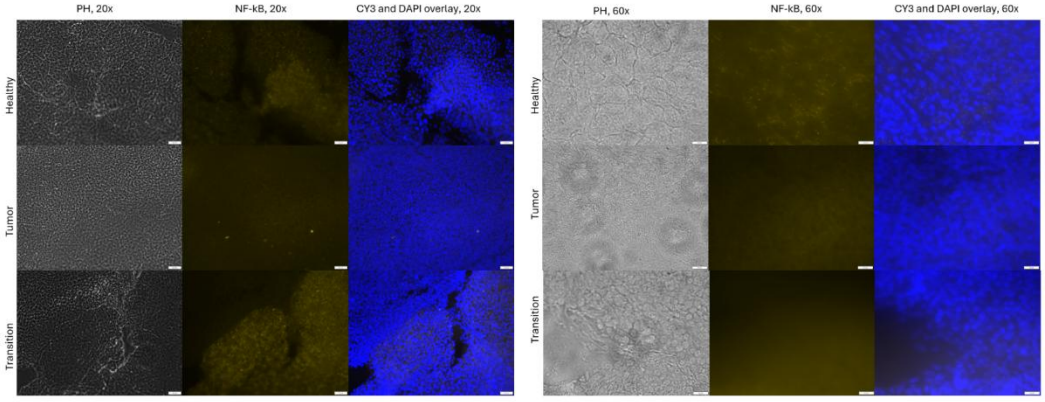

Figure 16 NFkB-Expression in MCT0969 treated with oxaliplatin. *Pictures were taken in 20x (scale bar: 50 µm) and 60x (scale bar: 20 µm) magnification and differentiated in healthy-, tumor- and transition-tissue. Here the expression seems to be stronger in the healthy pancreas section and in the healthy transition area which is observed as yellow staining in the affected cells (especially in the 60x magnification of the CY3 filter visible). The blue color of the cell nuclei from the DAPI-staining is visible in the CY3+DAPI overlay both 20x and 60x.*

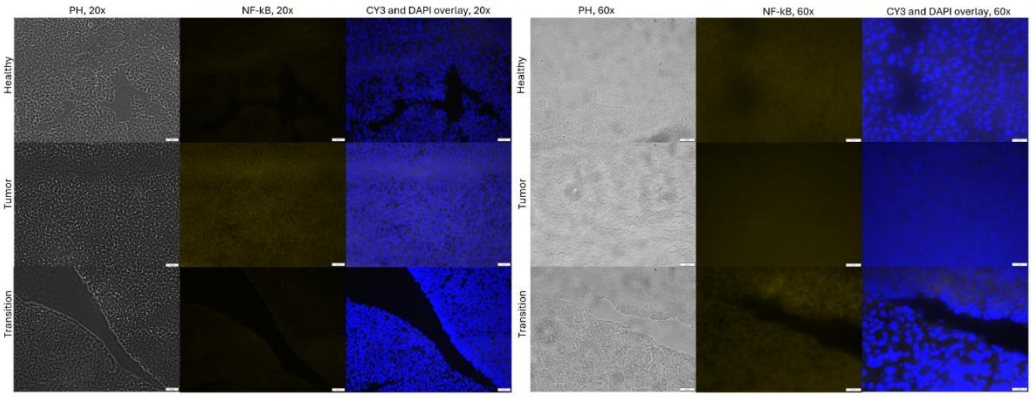

Figure 17 NFkB-Expression in MCT1171 NOT treated with oxaliplatin. *Pictures were taken in 20x (scale bar: 50 µm) and 60x (scale bar: 20 µm) magnification and differentiated in healthy-, tumor- and transition-tissue. The expression overall seems to be weak, since there are almost no NFkB signals (yellow stain) neither in the CY3-filter (20x and 60x) nor in the overlay with DAPI. The blue color of the cell nuclei from the DAPI-staining is visible in the CY3+DAPI overlay both 20x and 60x.*

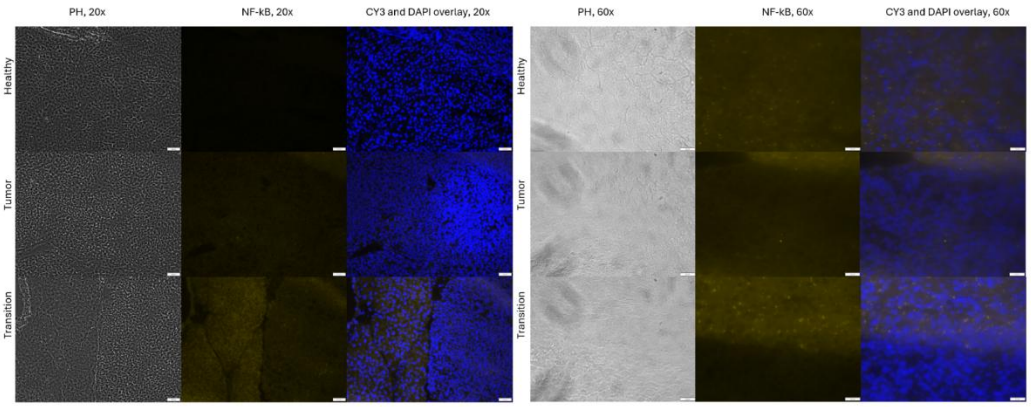

Figure 18 NFkB-Expression in MCT0957 NOT treated with oxaliplatin. *Pictures were taken in 20x (scale bar: 50 µm) and 60x (scale bar: 20 µm) magnification and differentiated in healthy-, tumor- and transition-tissue. In this case the 20x magnification shows a very weak expression as yellow stain is almost absent in the healthy and tumor area, the 60x magnification on the other hand has more signal spots. The signal seems to be subcellularly localized. The blue color of the cell nuclei from the DAPI-staining is visible in the CY3+DAPI overlay both 20x and 60x.*

7.1.3 TRAM1-Expression in Pancreatic Tissue

Upon staining with this antibody, it becomes immediately evident that TRAM1 expression in tumor tissue is very weak or entirely absent across all panels (**Figure 19-Figure 22**). In contrast, healthy tissue consistently exhibits strong fluorescence, indicative of high TRAM1 expression. While public databases indicate that TRAM1 is broadly expressed with low tissue specificity (Josephine Dubois, 2021), and low tumor specificity, some studies have found that TRAM1 is downregulated in cancer cells. (Sun, 2022) These results also suggest a potential context-dependent downregulation in the analyzed tumor samples. In these regions, the healthy portion maintains a strong signal, whereas the tumor area remains devoid of detectable TRAM1 expression.

Moreover, the localization of TRAM1 is particularly noteworthy. The signal is confined to the cell membrane, while no significant fluorescence is detected in the cytoplasm or nucleus. This contrasts with NFkB, which is as already mentioned commonly observed in nuclear compartments. The membrane-specific localization of TRAM1 is consistently visible in all images, facilitated by the clear definition of cell boundaries.

Despite these clear expression patterns, the apparent effect of oxaliplatin treatment in these mice (MCT1147, MCT0969, MCT1171 and MCT0957) is ambiguous. Across all images (**Figure 19-Figure 22**), there is no discernible difference in TRAM1 expression or fluorescence intensity between treated and untreated mice. This raises questions about the efficacy of the treatment in this experimental context or suggests that TRAM1 expression may not be significantly modulated by oxaliplatin in the analyzed tissue sections.

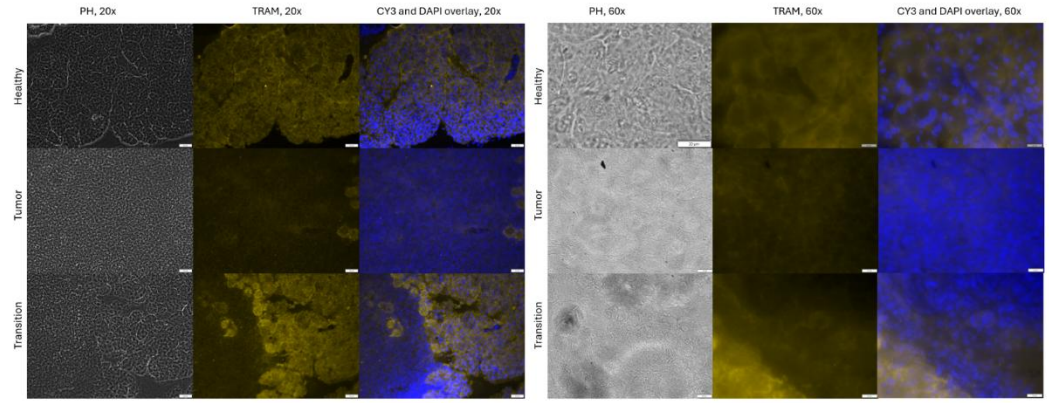

Figure 19 TRAM1-Expression in MCT1147 treated with oxaliplatin. *Pictures were taken in 20x (scale bar: 50 µm) and 60x (scale bar: 20 µm) magnification and differentiated in healthy-, tumor- and transition-tissue. The most noticeable feature is that there is no signal expression in the tumor section, as the panels visualizing the tumor area are very dark with very light shades of background stain. On the other hand, the 20x and 60x magnification show strong yellow staining in the whole cells in the healthy and transition areas. The blue color of the cell nuclei from the DAPI-staining is visible in the CY3+DAPI overlay both 20x and 60x.*

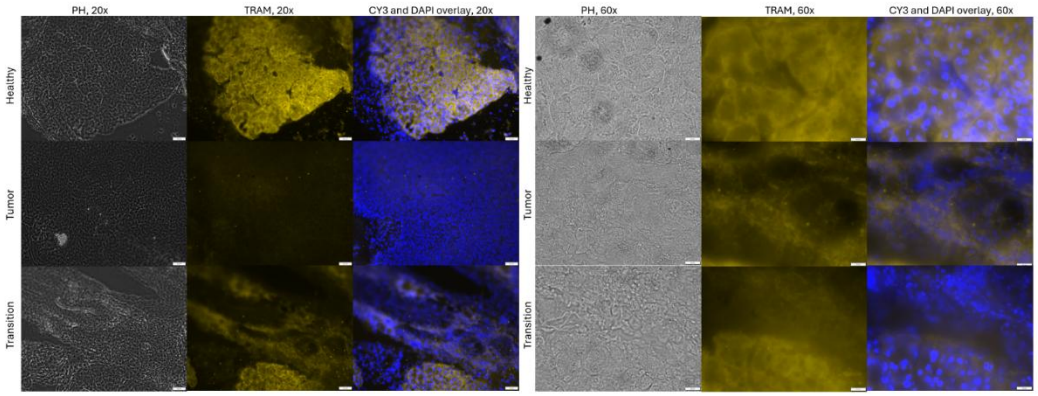

Figure 20 TRAM1-Expression in MCT0969 treated with oxaliplatin. *Pictures were taken in 20x (scale bar: 50 µm) and 60x (scale bar: 20 µm) magnification and differentiated in healthy-, tumor- and transition-tissue. The most noticeable feature is that there is no signal expression in the tumor section as the panels visualizing the tumor area are very dark with very light shades of background stain. But again, the 20x and 60x magnification show strong yellow staining in the whole cells in the healthy and transition areas. The blue color of the cell nuclei from the DAPI-staining is visible in the CY3+DAPI overlay both 20x and 60x.*

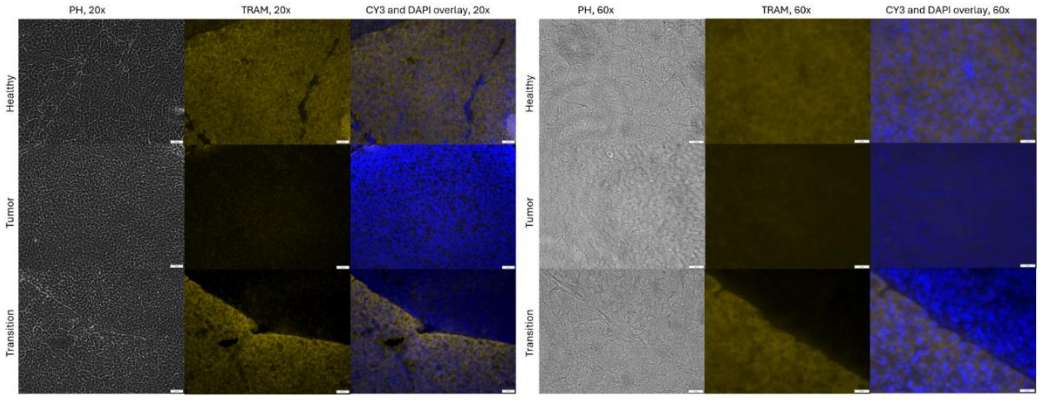

***Figure 21 TRAM1-Expression in MCT1171 NOT treated with oxaliplatin**. Pictures were taken in 20x (scale bar: 50 µm) and 60x (scale bar: 20 µm) magnification and differentiated in healthy-, tumor- and transition-tissue. The most noticeable feature is that there is no signal expression in the tumor section as the panels visualizing the tumor area are very dark with very light shades of background stain. the 20x and 60x magnification show strong yellow staining in the whole cells in the healthy and transition areas. The blue color of the cell nuclei from the DAPI-staining is visible in the CY3+DAPI overlay both 20x and 60x.*

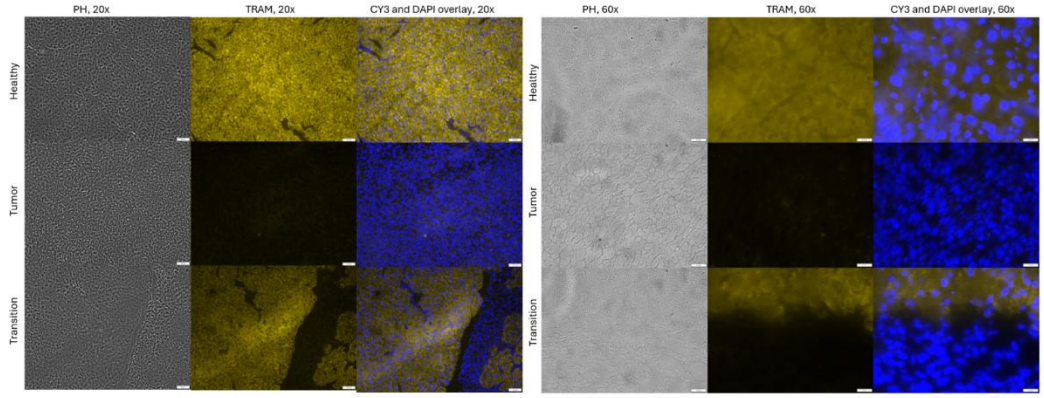

***Figure 22 TRAM1-Expression in MCT0957 NOT treated with oxaliplatin**. Pictures were taken in 20x (scale bar: 50 µm) and 60x (scale bar: 20 µm) magnification and differentiated in healthy-, tumor- and transition-tissue. The most noticeable feature is that there is no signal expression in the tumor section as the panels visualizing the tumor area are very dark with very light shades of background stain. the 20x and 60x magnification show strong yellow staining in the whole cells in the healthy and transition areas. The blue color of the cell nuclei from the DAPI-staining is visible in the CY3+DAPI overlay both 20x and 60x.*

7.1.4 MyD88-Expression in Pancreatic Tissue

The results of the MyD88 staining in this case indicate an overall very weak to absent expression. Some studies have shown an upregulation of expression—particularly in tumor regions of CRC suggesting that MyD88 may serve as a biomarker. (Thai Tra Dang, 2025) However, as shown in **Figure 23-Figure 25**, no clearly localized expression hotspots can be identified. Instead, the signal appears rather diffuse and unspecific, with most images showing predominantly background noise.

Furthermore, treatment with oxaliplatin does not appear to have a noticeable effect in this context, as no clear differences in MyD88 expression patterns can be observed between the treated mice MCT1147 and MCT0969 (**Figure 23** and **Figure 24**) and untreated mice MCT1171 and MCT0957 (**Figure 25-Figure 26**).

Possible explanations for these findings include that MyD88 may not be strongly expressed in the analyzed regions of this experiment, or that the sensitivity of the antibody used in this experiment was insufficient to detect low expression levels. Additionally, the relatively small sample size of four mice may limit the ability to draw definitive conclusions regarding MyD88 expression patterns.

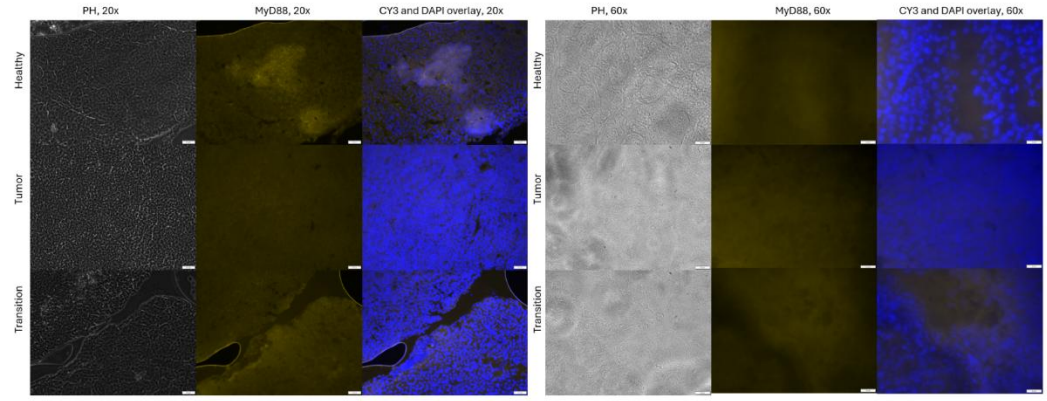

Figure 23 MyD88-Expression in MCT1147 treated with oxaliplatin. *Pictures were taken in 20x (scale bar: 50 µm) and 60x (scale bar: 20 µm) magnification and differentiated in healthy-, tumor- and transition-tissue. No specific expression-spots are visible in this section, since the only color visible in the CY3 panel in all the tissue areas in both magnifications is background. The blue color of the cell nuclei from the DAPI-staining is visible in the CY3+DAPI overlay both 20x and 60x.*

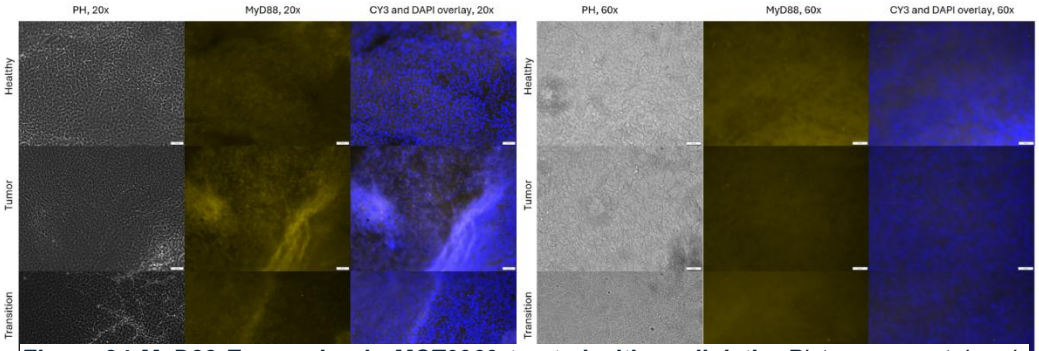

Figure 24 MyD88-Expression in MCT0969 treated with oxaliplatin*. Pictures were taken in 20x (scale bar: 50 µm) and 60x (scale bar: 20 µm) magnification and differentiated in healthy-, tumor- and transition-tissue. No specific expression-spots are visible in this section since the only color visible in the CY3 panel in all the tissue areas in both magnifications is background. The blue color of the cell nuclei from the DAPI-staining is visible in the CY3+DAPI overlay both 20x and 60x.*

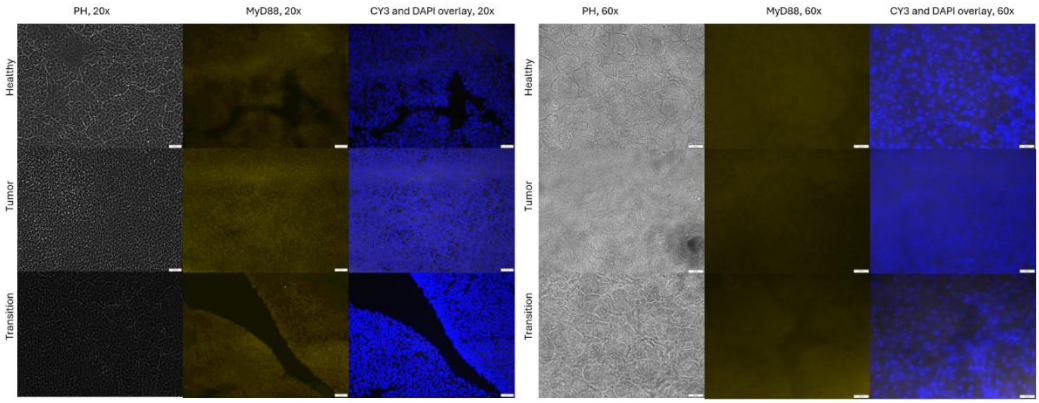

Figure 25 MyD88-Expression in MCT1171 NOT treated with oxaliplatin. *Pictures were taken in 20x (scale bar: 50 µm) and 60x (scale bar: 20 µm) magnification and differentiated in healthy-, tumor- and transition-tissue. In this case MyD88 expression is present as broad diffuse staining, as evidenced by yellow fluorescence in the cells of the tumor and transition sample in the 20x magnification. On the other hand, the 60x magnification shows only yellow background stain in the all the CY3 panels. The blue color of the cell nuclei from the DAPI-staining is visible in the CY3+DAPI overlay both 20x and 60x.*

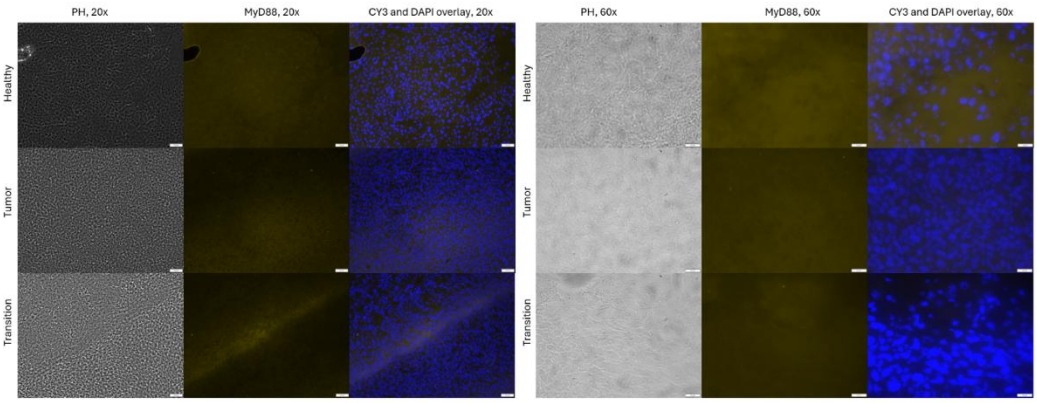

Figure 26 MyD88-Expression in MCT0957 NOT treated with oxaliplatin. *Pictures were taken in 20x (scale bar: 50 µm) and 60x (scale bar: 20 µm) magnification and differentiated in healthy-, tumor- and transition-tissue. No specific expression-spots are visible in this section since the only color visible in the CY3 panel in all the tissue areas in both magnifications is background. The blue color of the cell nuclei from the DAPI-staining is visible in the CY3+DAPI overlay both 20x and 60x.*

7.1.5 NFkB-Expression in Tumor Nodules

For the analysis of NFkB staining in tumor regions of the mouse models MCT1147, MCT0969, MCT1171, and MCT0957, it can be observed that the NFkB signal is overall highly punctate, with only a few distinct bright expression spots, while several areas remain completely devoid of signal. This pattern suggests that NFkB is not globally activated but rather restricted to individual cells.

A particularly striking observation is the apparent NFkB staining pattern detected in MCT1147 (**Figure 27**) at 60x magnification in FOV1. However, upon reevaluation, this signal does not appear to represent a true biological NFkB activation but rather resembles an antibody-related artefact. In contrast, MCT0969 shows multiple smaller punctate spots, yet similarly lacks evidence of a strong, specific activation signal as illustrated in **Figure 28**. Overall, these findings suggest that NFkB activation is not convincingly supported across the examined samples, and the observed staining pattern is likely attributable to non-specific antibody binding rather than genuine pathway activation.

On the other hand, the untreated mice (**Figure 29** and **Figure 30**) also display occasional NFkB-positive signals, some of which are comparable to those observed in treated samples. In this case, no clear effect of oxaliplatin treatment can be identified again.

In comparison to the pancreatic tissue described above, which was analyzed for NFkB expression, this overall weak signal is not unexpected. As previously observed, tumor regions were largely negative for NFkB expression, whereas expression in pancreatic tissue and transitional areas was notably upregulated. Since the sections only contain tumor tissue, the pictures were taken in 2 different fields of view in 20x and 60x magnification.

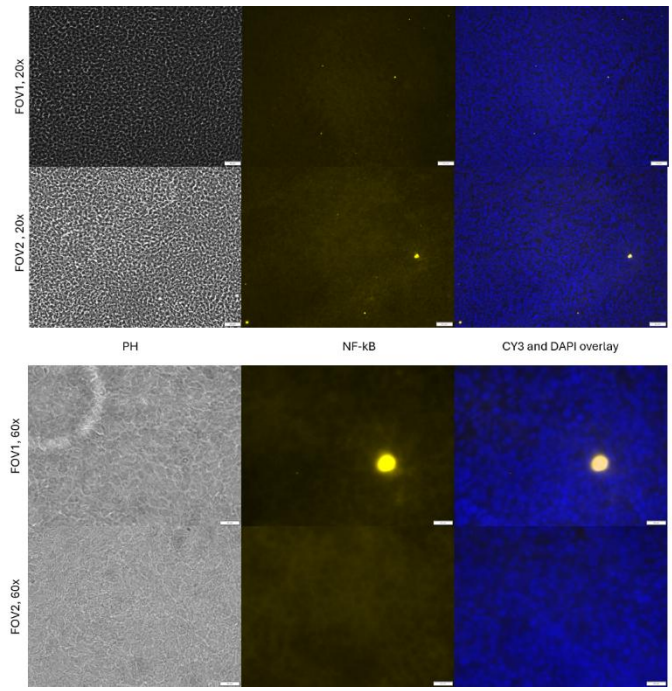

Figure 27 NFkB-Expression in MCT1147 treated with oxaliplatin. *Pictures were taken in 20x (scale bar: 50 µm) and 60x (scale bar: 20 µm) magnification in 2 different FOVs. The 20x magnification in FOV1 and FOV2 show small but visible expression spots via yellow puncta. But only big bright yellow signal in FOV1 in 60x is visible. The blue color of the cell nuclei from the DAPI-staining is visible in the CY3+DAPI overlay both 20x and 60x.*

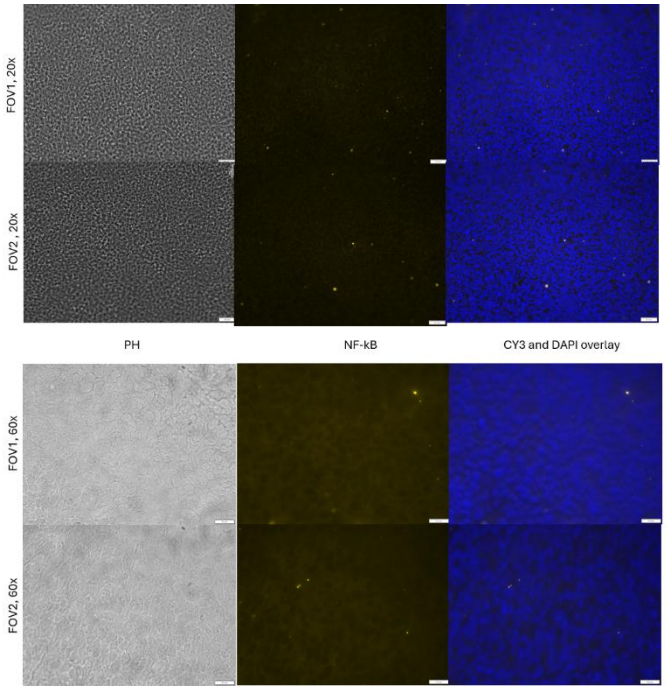

Figure 28 NFkB-Expression in MCT0969 treated with oxaliplatin. *Pictures were taken in 20x (scale bar: 50 µm) and 60x (scale bar: 20 µm) magnification in 2 different FOVs. The 20x magnification in FOV1 and FOV2 show diffusely distributed yellow spots. Same goes for the 60x magnification. The blue color of the cell nuclei from the DAPI-staining is visible in the CY3+DAPI overlay both 20x and 60x.*

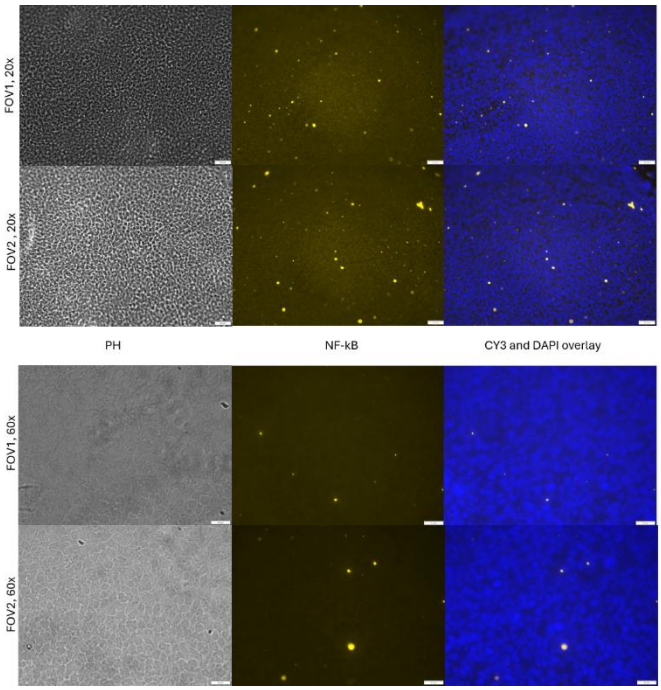

***Figure 29 NFkB-Expression in MCT1171 NOT treated with oxaliplatin**. Pictures were taken in 20x (scale bar: 50 µm) and 60x (scale bar: 20 µm) magnification in 2 different FOVs. The 20x magnification in FOV1 and FOV2 show many diffusely distributed yellow spots. Equally, the 60x magnification shows a few expression spots. The blue color of the cell nuclei from the DAPI-staining is visible in the CY3+DAPI overlay both 20x and 60x.*

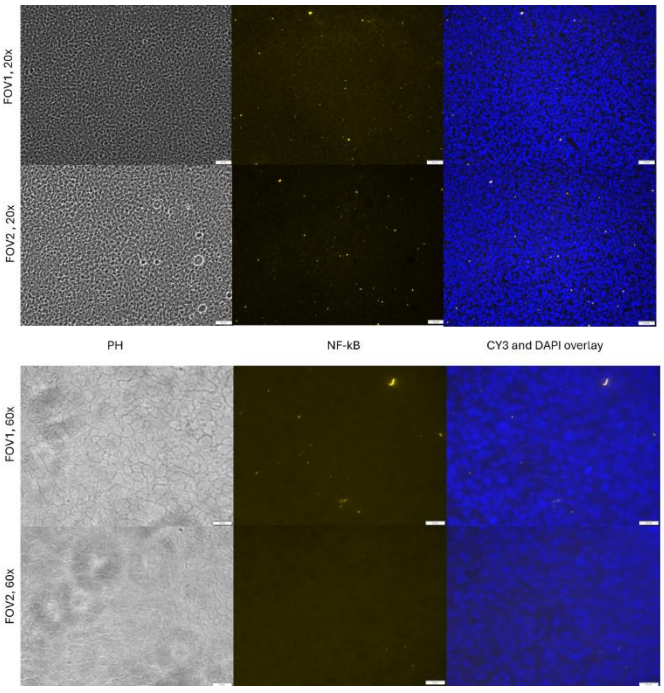

***Figure 30 NFkB-Expression in MCT0969 NOT treated with oxaliplatin**. Pictures were taken in 20x (scale bar: 50 µm) and 60x (scale bar: 20 µm) magnification in 2 different FOVs. The 20x magnification in FOV1 and FOV2 exhibit small and weak yellow spots. FOV1 of the 60x magnification also shows a few small signals. The blue color of the cell nuclei from the DAPI-staining is visible in the CY3+DAPI overlay both 20x and 60x.*

7.1.6 TRAM1-Expression of the Tumor Nodules

As already expected from the previous section 7.1.2, the immunofluorescence analysis of TRAM1 expression on tumor nodules reveals no detectable expression signal in tumor regions across all the samples investigated. (**Figure 31-Figure 34**) This observation is consistent in both oxaliplatin-treated and untreated conditions, as well as across different mice used (MCT1147, MCT0969, and MCT0957). This again confirms the lack of effect of oxaliplatin in the treated vs. untreated mice.

While DAPI staining confirms the presence of nuclei and overall cell integrity, TRAM1-specific fluorescence remains absent or limited to weak, diffuse background staining without clear subcellular localization.

These findings suggest that TRAM1 is either not expressed or expressed below detection levels in the analyzed tumor sections, independent of chemotherapeutic treatment.

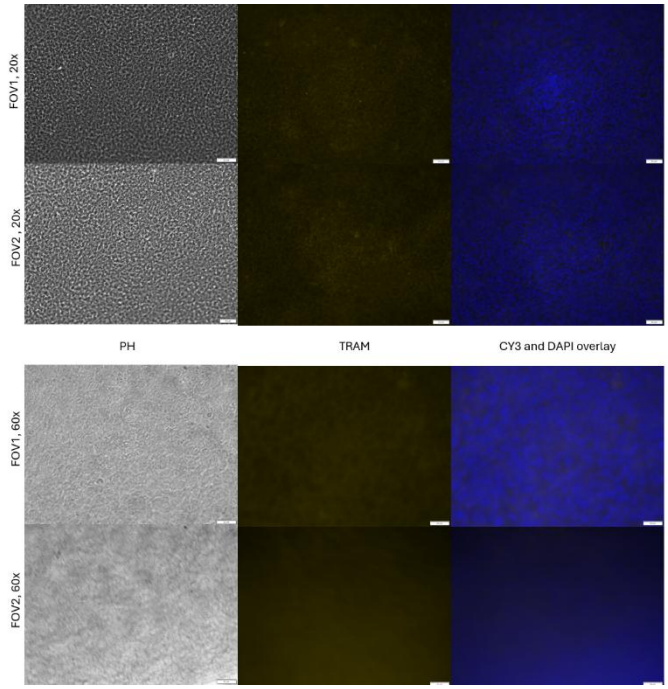

***Figure 31 TRAM1-Expression in MCT1147 treated with oxaliplatin**. Pictures were taken in 20x (scale bar: 50 µm) and 60x (scale bar: 20 µm). The most noticeable feature is that there is no signal expression in form of yellow stain in all of the tumor sections as all the CY3 panels remain dark. The blue color of the cell nuclei from the DAPI-staining is visible in the CY3+DAPI overlay both 20x and 60x.*

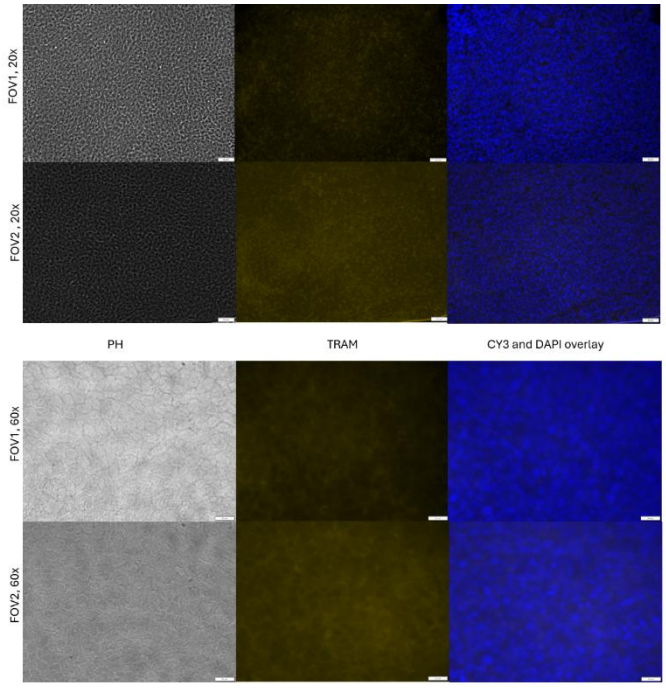

Figure 32 TRAM1-Expression in MCT0969 treated with oxaliplatin. *Pictures were taken in 20x (scale bar: 50 µm) and 60x (scale bar: 20 µm). The most noticeable feature is that there is no signal expression in form of yellow stain in all of the tumor sections as all the CY3 panels remain dark. The blue color of the cell nuclei from the DAPI-staining is visible in the CY3+DAPI overlay both 20x and 60x.*

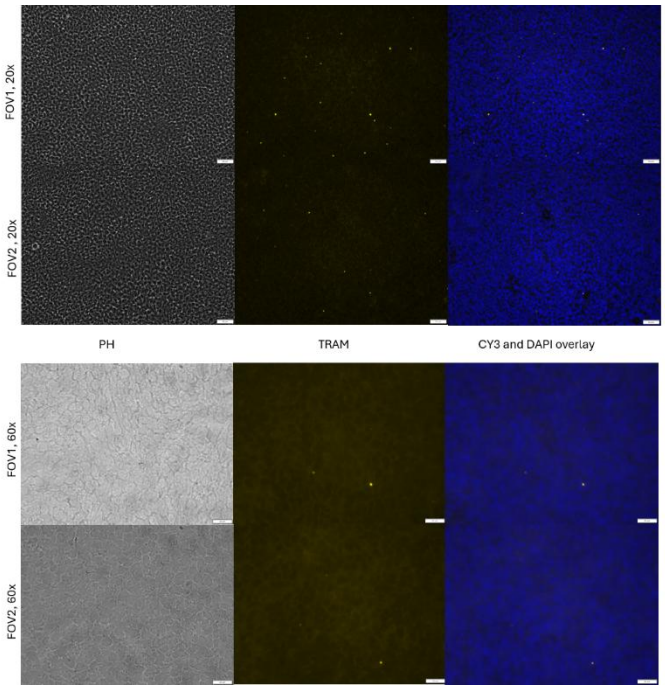

Figure 33 TRAM1-Expression in MCT1171 NOT treated with oxaliplatin*. Pictures were taken in 20x (scale bar: 50 µm) and 60x (scale bar: 20 µm). The most noticeable feature is that there is no signal expression in form of yellow stain in all of the tumor sections as all the CY3 panels remain dark. The blue color of the cell nuclei from the DAPI-staining is visible in the CY3+DAPI overlay both 20x and 60x.*

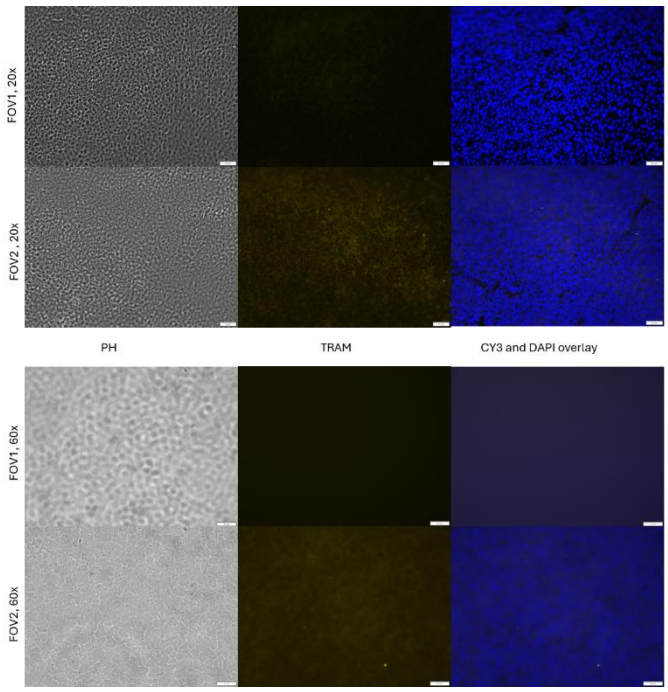

Figure 34 TRAM1-Expression in MCT0957 NOT treated with oxaliplatin. *Pictures were taken in 20x (scale bar: 50 µm) and 60x (scale bar: 20 µm). The most noticeable feature is that there is no signal expression in form of yellow stain in all of the tumor sections as all the CY3 panels remain dark. The blue color of the cell nuclei from the DAPI-staining is visible in the CY3+DAPI overlay both 20x and 60x.*

7.1.7 MyD88-Expression of Tumor Nodules

The immunofluorescence staining with MyD88 in tumor nodules reveals the presence of MyD88 expression in most of the examined samples, although the signal is sparse and appears as discrete spots rather than a uniform distribution. For example, **Figure 35** in and **Figure 36** only a few weak spots can be detected, however they do not really appear to be related. These punctate signals are also observed across untreated groups (**Figure 37** and **Figure 38**), since the pictures show a few weak signals but no consistent expression pattern. Again, no conclusion can be drawn as to whether oxaliplatin influences the expression or not.

Notably, a high degree of heterogeneity is observed between different fields of view and magnifications. While some regions display only minimal expression (**Figure 35**, FOV1), others exhibited isolated but strong fluorescence signals

(**Figure 35**, FOV2, 60x). However, this strong signal is attributed to what seems to be an artefact of antibodies.

However, DAPI staining confirms the presence of intact nuclei, indicating that the observed variability in MyD88 signal is unlikely due to technical artifacts.

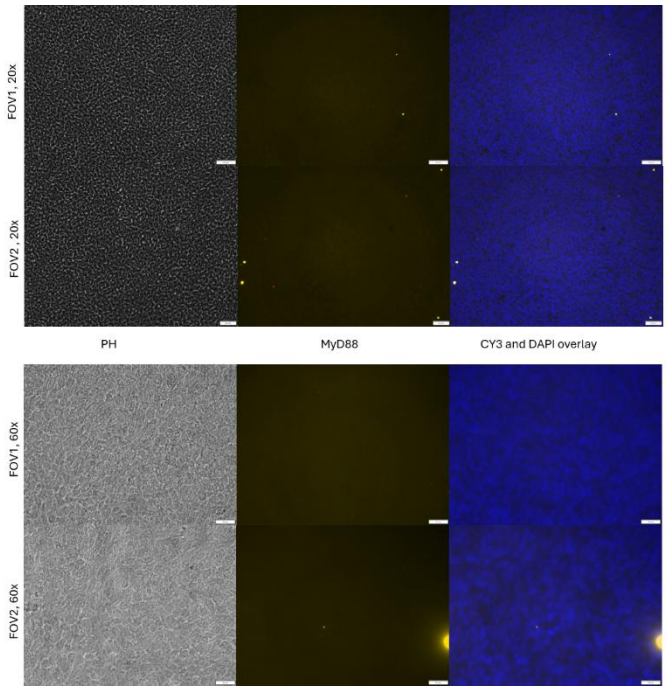

***Figure 35 MyD88-Expression in MCT1147 treated with oxaliplatin**. Pictures were taken in 20x (scale bar: 50 µm) and 60x (scale bar: 20 µm). The 20x magnification in FOV1 and FOV2 almost lack yellow expression spots and the few puncta that are visible are very small, weak and unevenly distributed. Only one signal in FOV1 in 60x is visibly bright yellow. The blue color of the cell nuclei from the DAPI-staining is visible in the CY3+DAPI overlay both 20x and 60x.*

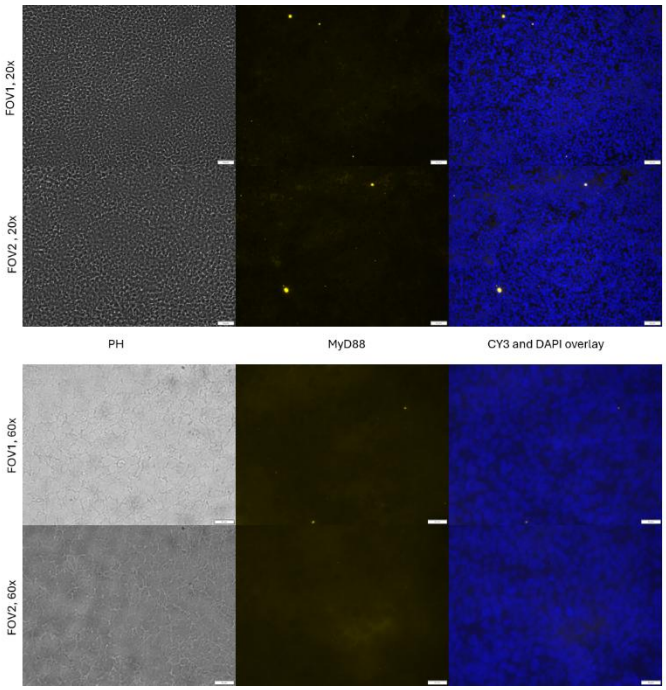

***Figure 36 MyD88-Expression in MCT0969 treated with oxaliplatin**. Pictures were taken in 20x (scale bar: 50 µm) and 60x (scale bar: 20 µm). The 20x magnification in FOV1 and FOV2 almost lack yellow expression spots and the few puncta that are visible are very small, weak and unevenly distributed. On the other hand, 60x magnification does not show any expression. The blue color of the cell nuclei from the DAPI-staining is visible in the CY3+DAPI overlay both 20x and 60x.*

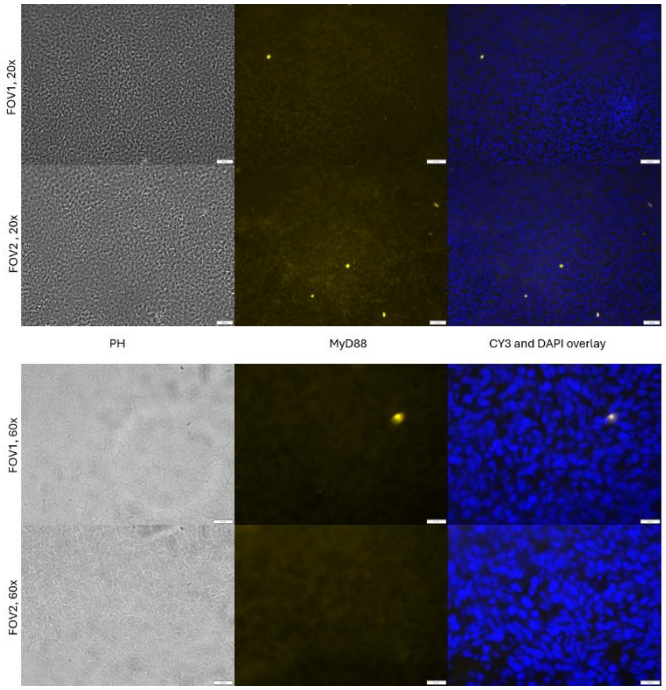

***Figure 37 MyD88-Expression in MCT1171 NOT treated with oxaliplatin**. Pictures were taken in 20x (scale bar: 50 µm) and 60x (scale bar: 20 µm). The 20x magnification in FOV1 and FOV2 almost lack yellow expression spots and the few puncta that are visible are very small, weak and unevenly distributed. Even the 60x magnification in FOV1 shows only 2 expression spots. The blue color of the cell nuclei from the DAPI-staining is visible in the CY3+DAPI overlay both 20x and 60x.*

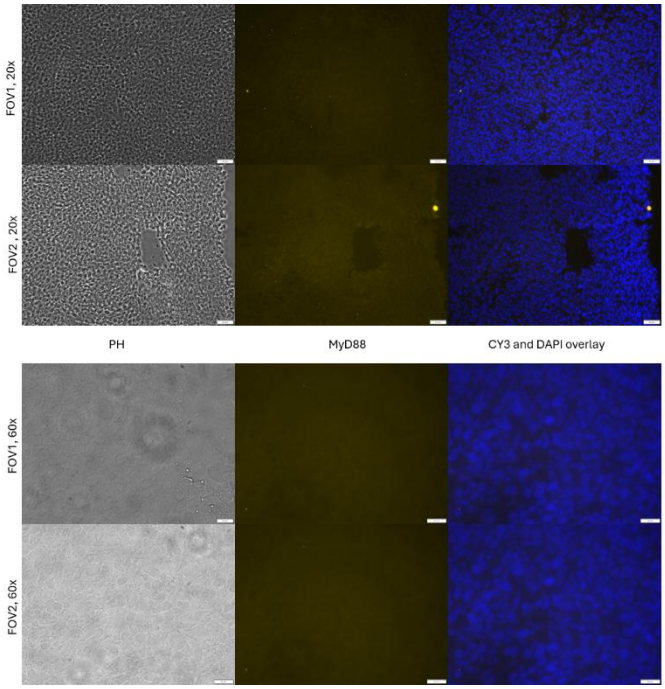

Figure 38 MyD88-Expression in MCT1171 NOT treated with oxaliplatin. *Pictures were taken in 20x (scale bar: 50 µm) and 60x (scale bar: 20 µm). In this case the 20x and 60x magnification of FOV1 and FOV2 remains dark without any yellow expression spots in the CY3 panels. The blue color of the cell nuclei from the DAPI-staining is visible in the CY3+DAPI overlay both 20x and 60x.*

7.2 Results of the HRP-Staining of the Mouse Project

The HRP-based immunohistochemical staining was performed to assess the expression of HIF1α in the CT26 Luc tumor models which have treatment conditions, as already mentioned. Tissue sections were categorized again into healthy, tumor, and transition regions, and both isotype controls and HIF1α-stained samples were analyzed to ensure specificity of staining.

Overall, the isotype controls display minimal background staining across all samples (**Figure 39-Figure 40**), confirming the specificity of the antibody and the reliability of the observed HIF1α signals. In contrast, HIF1α-stained sections exhibited varying intensities of brown chromogenic signal, indicating differences in protein expression depending on tissue type and treatment condition. (**Figure 39**)

In **Figure 39** MCT1147, shows a clear difference to the untreated mice. The tumor region of MCT1147 shows a noticeably stronger HIF1α signal compared to untreated controls, whereas healthy tissue consistently exhibited weak or negligible staining. Transition zones display intermediate staining intensities, suggesting a gradual shift in HIF1α expression between healthy and malignant tissue. These findings indicate that oxaliplatin treatment may be associated with an upregulation of HIF1α in this tumor model.

In contrast, the MCT0969 and MCT0957 models show a less pronounced and more heterogeneous pattern. While some treated samples exhibit moderate HIF1α expression, the differences between treated and untreated tissues were not as distinct as in the MCT1147 model. In these cases, staining appeared more variable, with some regions displaying only weak signal intensity regardless of treatment. This suggests that the response to oxaliplatin may be model-dependent and influenced by intrinsic tumor characteristics.

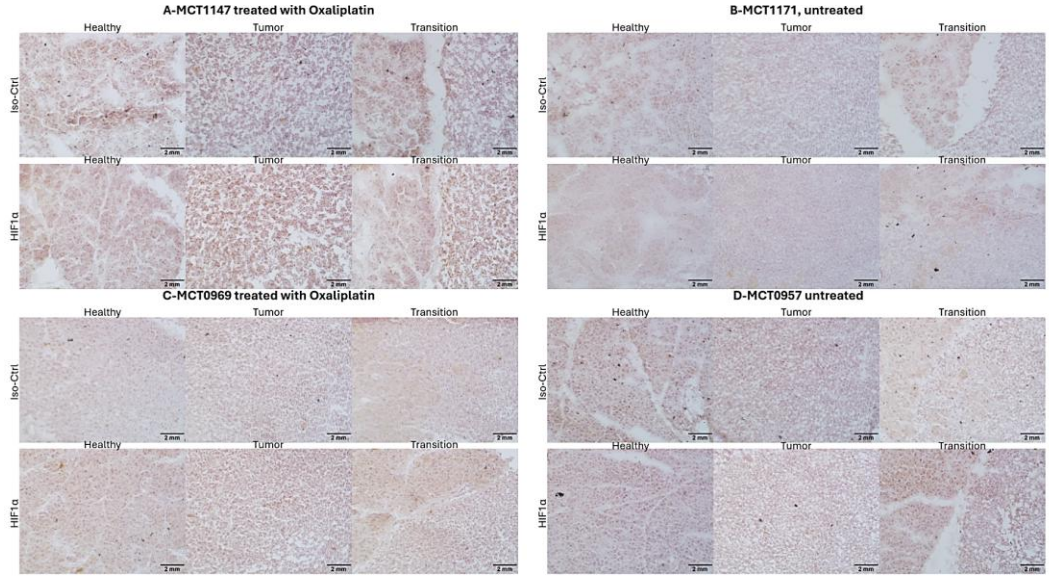

Figure 39 Comparison of HRP staining in MCT1147 (A), MCT1171 (B) – both treated with oxaliplatin, MCT0969 (C) and MCT0957 D – both left untreated in 20x *(scale bar: 2 mm). Tissue regions were classified as healthy, tumor, or transition. For each mouse, both the isotype control and HIF1α-stained samples are presented. There seems to be a slight difference in expression of HIF1α between the treated (A and C) section and untreated (B and C) section. The tissue of the treated mice shows slightly more brown color, meaning there is more expression in HIF1α.*

Overall, the staining patterns in the tumor nodules (**Figure 40**) confirm the observations made in the mixed sections. In the oxaliplatin treated groups, particularly in the MCT1147, tumor sections exhibit a relatively uniform but moderately increased HIF1α staining compared to untreated counterparts. Although the signal intensity is not as strongly contrasted as in the mixed tissue sections, a consistent presence of HIF1α could be observed across multiple fields of view, indicating that the treatment-associated upregulation is retained within the tumor itself.

In untreated tumors, staining appeared more heterogeneous and, in some cases, slightly weaker overall. Though localized regions of higher intensity were still detectable. This suggests that even in the absence of treatment, baseline HIF1α expression varies within the tumor microenvironment, likely reflecting differences in oxygen availability and cellular composition.

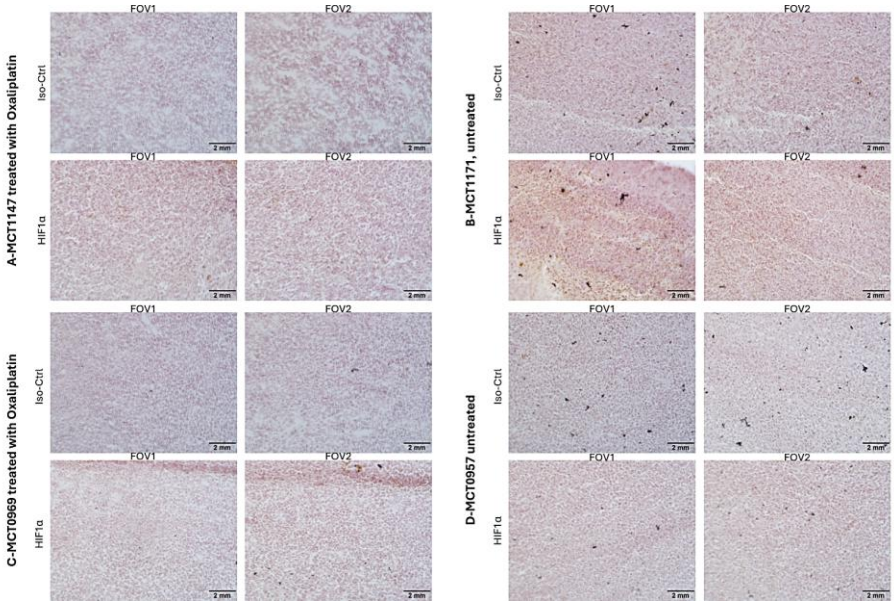

Figure 40 Comparison of HRP staining in MCT1147 (A), MCT1171 (B) – both treated with oxaliplatin, MCT0969 (C) and MCT0957 D – both left untreated in 20x *(scale bar: 2 mm). The pictures were taken in 2 different FOVs. Tumor sections from oxaliplatin-treated groups display a relatively increased HIF1α staining compared to untreated counterparts, since the HIF1α stained regions exhibit a darker shade of brown throughout the tumor regions. In contrast, untreated tumors exhibit more heterogeneous and occasionally weaker staining.*

7.3 Results of the IHC-Staining in Spheroids

The following images show the stained spheroids that were harvested on days 7 and 8. Due to the high level of stress experienced by the spheroids, many cellular compartments were lost during the staining process, and a large number of entire spheroids were completely destroyed.

As described above in the Materials and Methods section, one slide was prepared for each spheroid type (treated with 25 mM and 100 mM oxaliplatin, untreated, and from days 7 and 8), each containing four rows with three spheroids per row. Therefore, the results would ideally display three spheroids per condition. However, only two spheroids per treatment are shown.

This selection of images was made to ensure a uniform and representative presentation, as the remaining spheroids were destroyed during the process.

7.3.1 NFkB-Expression in Spheroids of D7 and D8

Although many cellular compartments of the spheroids were destroyed during the staining process, several meaningful observations can still be derived from the results. The spheroids harvested on day 7 and stained with NFkB demonstrate that the concentration of added oxaliplatin has a pronounced effect on the distribution and intensity of the signal. Despite the loss of some structural integrity and cellular compartments due to stress during harvesting and staining, clear differences between treatment groups are still evident.

Examining the images, block C (**figure 41** sp1 and sp2 +100 mM oxaliplatin) appears to exhibit the most intense signal, with numerous bright spots distributed throughout the spheroid at both 20x and 60x magnification. At first glance, this could suggest elevated NFkB activity associated with the higher oxaliplatin dose. However, the signal pattern is somewhat irregular and punctate, raising the possibility that at least part of the staining represents antibody aggregates rather than entirely specific NFkB expression.

In contrast, the untreated control spheroids and those treated with 25 mM oxaliplatin display relatively few visible spots. While this difference might indicate a dose-dependent increase in NFkB expression, the potential contribution of non-specific staining in the high-dose condition complicates this interpretation.

Overall, although a trend toward stronger signal intensity at higher oxaliplatin concentrations can be observed, the presence of likely antibody aggregates reduces confidence in the specificity of the signal. Therefore, while the staining still permits a degree of comparative analysis across conditions, the results should be interpreted with caution. Additional controls or optimization of the staining protocol would be necessary to confirm whether the observed increase in signal truly reflects a dose-dependent upregulation of NFkB activity.

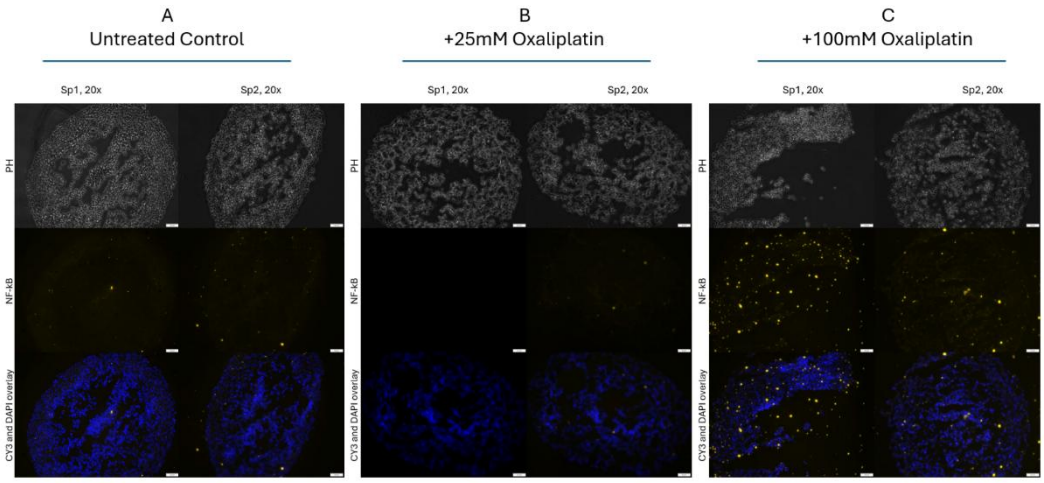

Figure 41 NFkB-Expression in Spheroid 1 and 2 of D7. *Representative images of untreated control spheroids (A) compared to spheroids treated with 25 mM (B) and 100 mM oxaliplatin (C), in 20x (magnification 50 µm). The strongest expression is visible in the Sp1 and Sp2 treated with 100mM oxaliplatin as visualized by the many small yellow spots, yet they seem to be not evenly distributed. The other two blocks (A and B) only show almost black CY3 panels with only few very weak signal spots. The blue color of the cell nuclei from the DAPI-staining is visible in the CY3+DAPI overlay.*

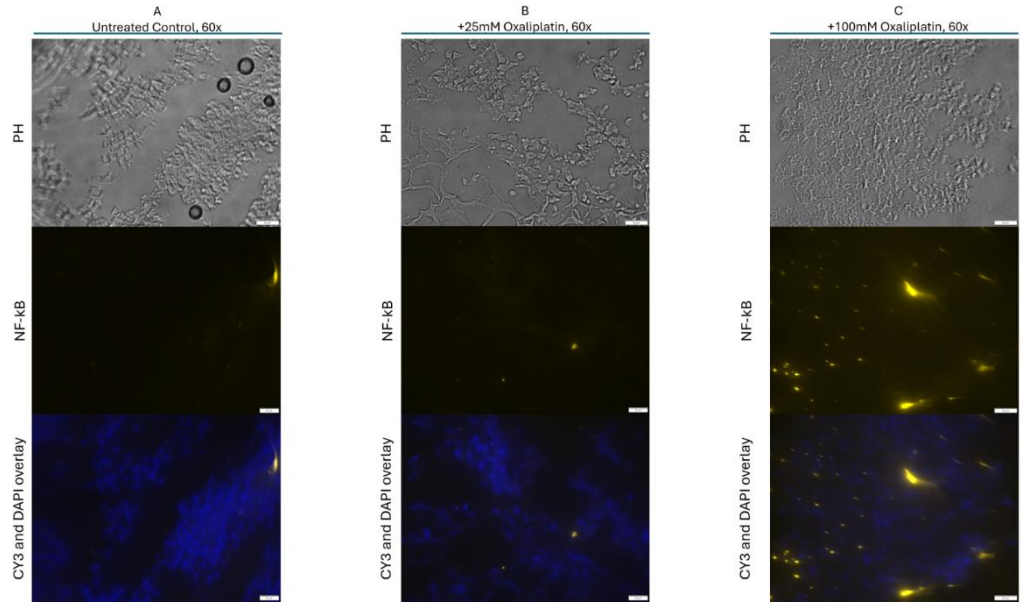

Figure 42 NFkB-Expression in the most representative spheroid of D7. *Representative images of untreated control spheroids (A) compared to spheroids treated with 25 mM (B) and 100 mM oxaliplatin (C), in 60x magnification (scale bar: 20 µm). Again, the C block has the strongest expression visualizing yellow stain throughout the CY3 panel and the CY3+DAPI overlay. However, these spots seem to be antibody aggregates. The blue color of the cell nuclei from the DAPI-staining is visible in the CY3+DAPI overlay.*

It should be noted that only one spheroid in the untreated control group (**Figure 43** A) survived the staining; therefore, no Sp2 results are visible at 20x magnification.

Nevertheless, NFkB appears to show strong expression in the treated spheroids in the available images. In particular, group C (**Figure 43**, C +100 mM oxaliplatin) seems to again in this case exhibit slightly stronger expression than the spheroid treated with 25 mM, which is noticeable at 60x magnification. In image 20 of group C, several spots are visible, including two prominent, intense expression spots.

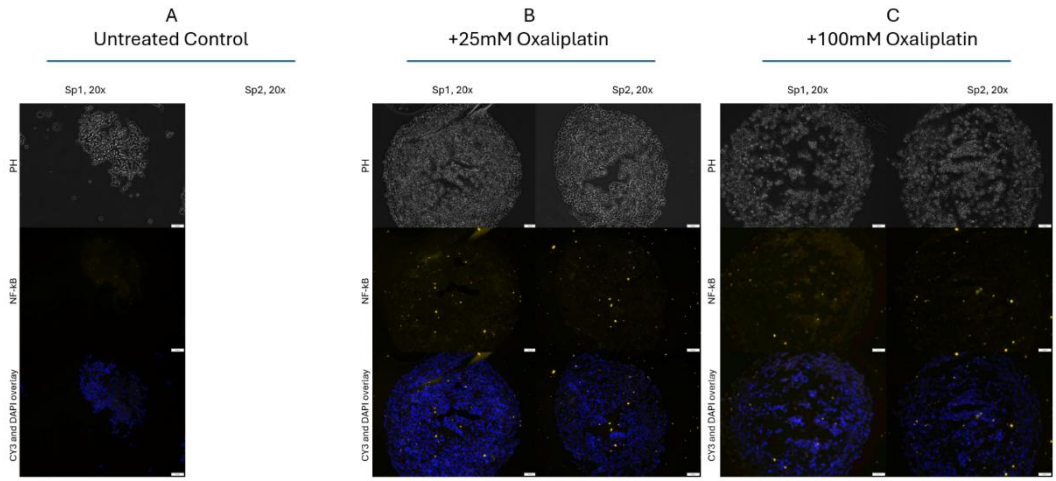

Figure 43 NFkB-Expression in Spheroid 1 and 2 of D8. *Representative images of untreated control spheroids (A) compared to spheroids treated with 25 mM (B) and 100 mM oxaliplatin (C), in 20x magnification (magnification 50 µm). It is important to note that Sp2 of block A was destroyed during the staining process, therefor no results can be shown. Some yellow spots are visible in the B and C block in contrast to the A block, which might be because the Sp1 is mostly destroyed. The blue color of the cell nuclei from the DAPI-staining is visible in the CY3+DAPI overlay.*

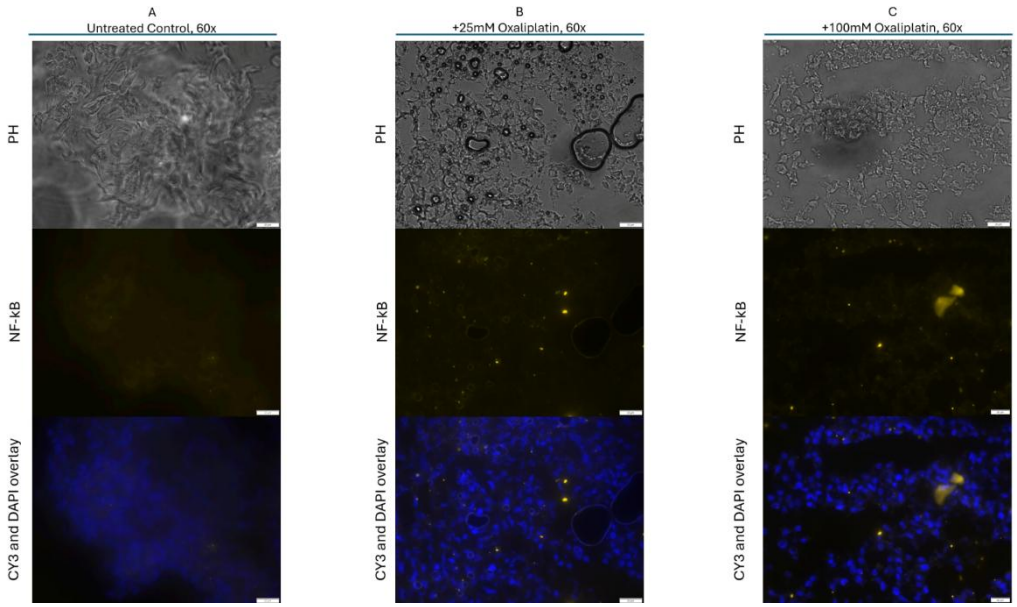

Figure 44 NFkB-Expression in the most representative spheroid of D8. *Representative images of untreated control spheroids (A) compared to spheroids treated with 25 mM (B) and 100 mM oxaliplatin (C), in 60x magnification (scale bar: 20 µm). Again, no expression in block A, as the CY3 panel remains black. But in block C of this magnification one distinct, strong yellow signal stands out. The blue color of the cell nuclei from the DAPI-staining is visible in the CY3+DAPI overlay.*

7.3.2 TRAM1-Expression in Spheroids D7 and D8

As already discussed in the previous chapters regarding TRAM1 expression in pancreatic tissue and in tumor nodules, TRAM1 is also not expressed in the spheroids here. This is made visible **Figure 45** and **Figure 46**. This result is expected, since TRAM1 is only expressed in healthy cells (Sun, 2022), and spheroids are known to consist of CT26 colon carcinoma cells. Likewise, the presence of oxaliplatin and the increase in dose from 25 mM to 100 mM appear to have no effect on the TRAM1 expression signal, as all images in the CY3 channel remain dark.

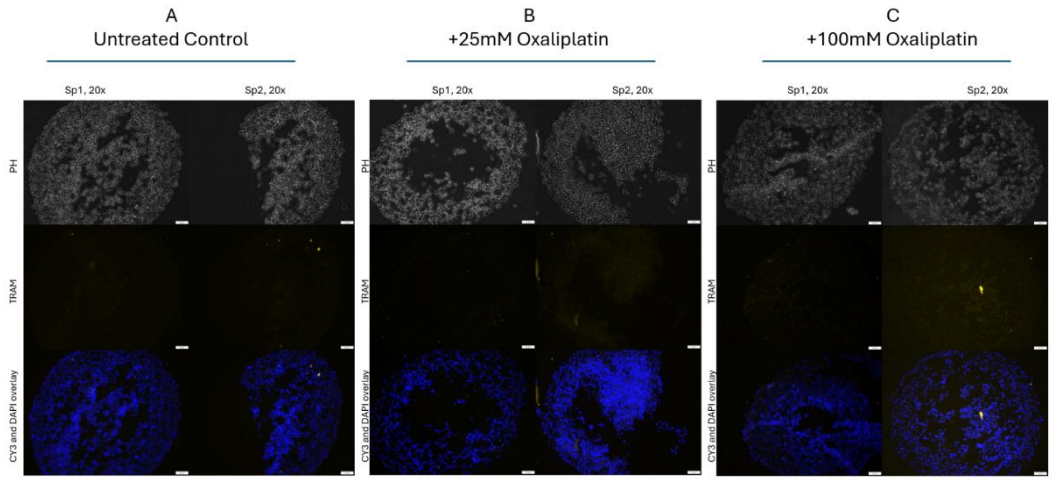

Figure 45 TRAM1-Expression in Spheroid 1 and 2 of D7. *Representative images of untreated control spheroids (A) compared to spheroids treated with 25 mM (B) and 100 mM oxaliplatin (C), in 20x magnification (scale bar: 50 µm). Almost no expression is visible in either of the blocks, since the CY3 panel across all 3 blocks is black obtaining any yellow stain. The blue color of the cell nuclei from the DAPI-staining is visible in the CY3+DAPI overlay.*

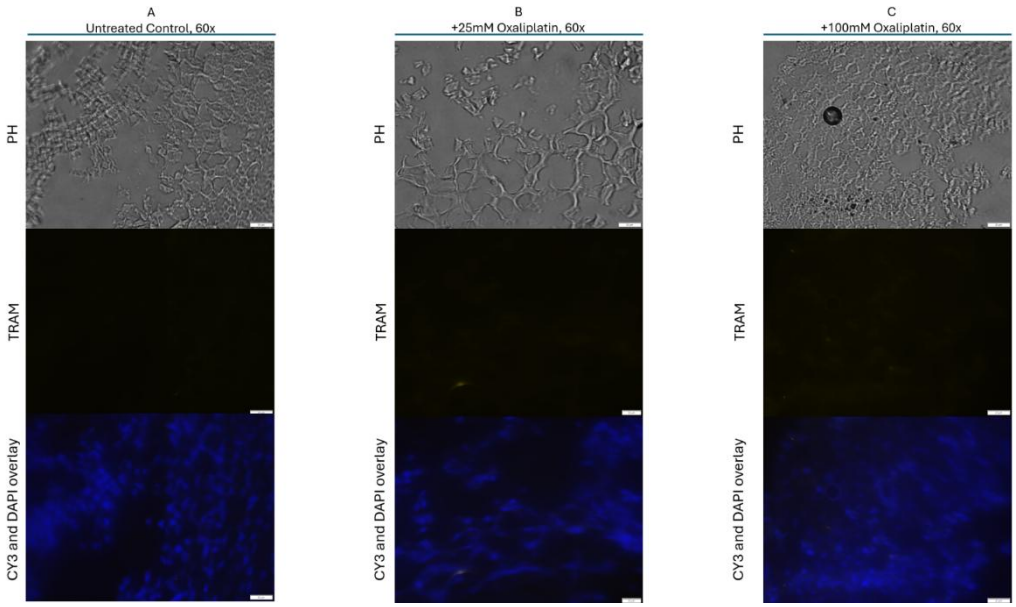

Figure 46 TRAM1-Expression in the most representative spheroid of D7. *Representative images of untreated control spheroids (A) compared to spheroids treated with 25 mM (B) and 100 mM oxaliplatin (C), in 60x magnification (scale bar: 20 µm). Almost no expression is visible in either of the blocks, since the CY3 panel across all 3 blocks is black obtaining any yellow stain. The blue color of the cell nuclei from the DAPI-staining is visible in the CY3+DAPI overlay.*

Unfortunately, in this case (**Figure 47** and **Figure 48**) the control did not survive the staining process, therefore no significant results can be shown. Still, one can see that the expression of TRAM1 in spheroids harvested on D8 equally as on D7, is not existent. The results here, are therefore equivalent to the previous section “TRAM1-Expression in Spheroids of D7”.

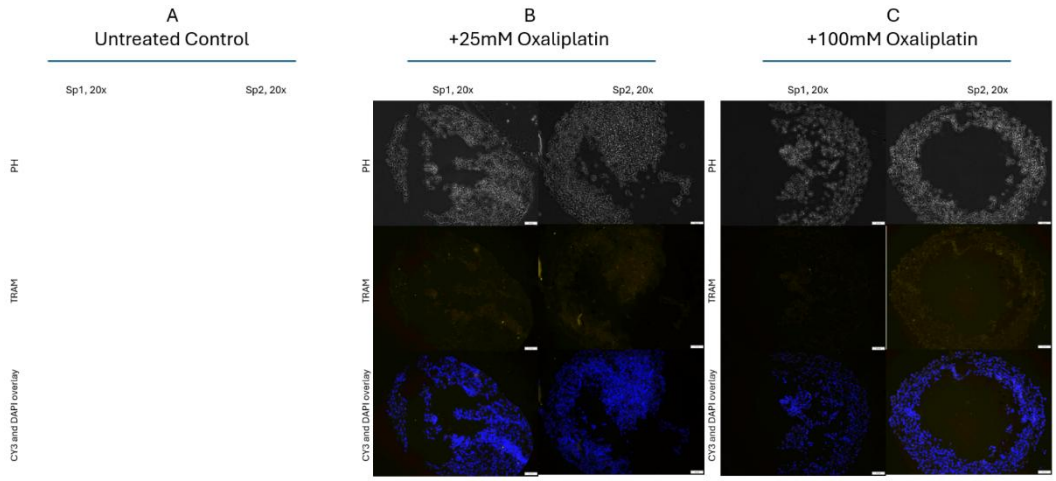

Figure 47 TRAM1-Expression in Spheroid 1 and 2 of D8. *Representative images of untreated control spheroids (A) compared to spheroids treated with 25 mM (B) and 100 mM oxaliplatin (C), in 20x magnification (scale bar: 50 µm). It is important to note that Sp1 and Sp2 of block A were destroyed during the staining process, therefor no results can be shown. Almost no expression is visible in either of the blocks, since the CY3 panel across all 3 blocks is black obtaining any yellow stain. The blue color of the cell nuclei from the DAPI-staining is visible in the CY3+DAPI overlay.*

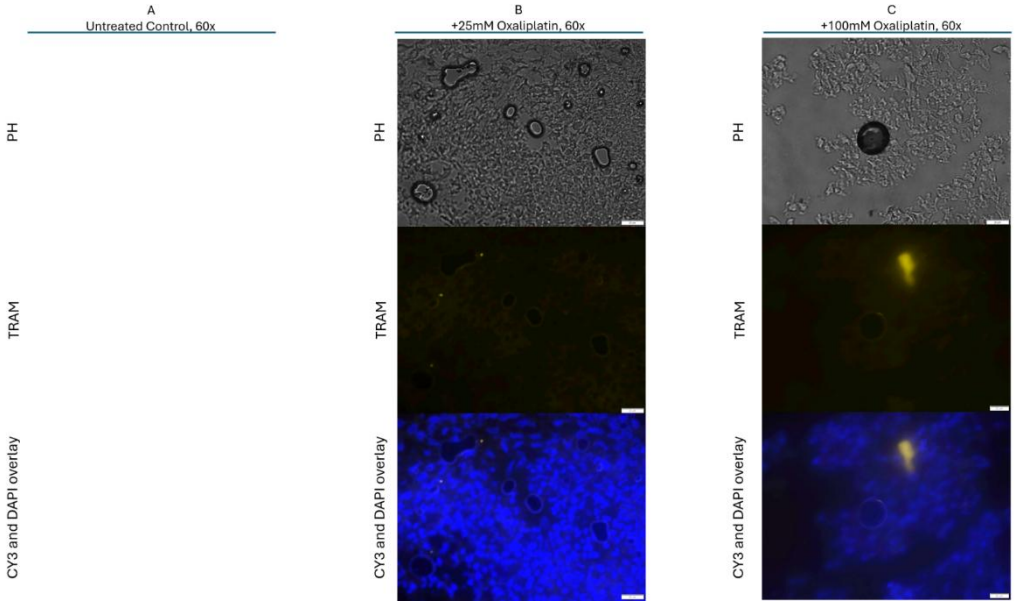

Figure 48 TRAM1-Expression in the most representative spheroid of D8. *Representative images of untreated control spheroids (A) compared to spheroids treated with 25 mM (B) and 100 mM oxaliplatin (C), in 60x magnification (scale bar: 20 µm). It is important to note that Sp1 and Sp2 of block A were destroyed during the staining process, therefor no results can be shown. Almost no expression is visible in either of the blocks, since the CY3 panel across all 3 blocks is black obtaining any yellow stain. The blue color of the cell nuclei from the DAPI-staining is visible in the CY3+DAPI overlay.*

7.3.3 MyD88-Expression in Spheroids of D7 and D8

In this case, the use of MyD88 on the spheroids shows very little expression **(Figure 49-Figure 50).** Similar to the MYD88 results discussed above in the mouse project, no distinct expression pattern is observed here, as expression appears sporadic, weak, and heterogeneous in both treated and untreated spheroids. This behavior of MyD88 does not seem to result from the stressed state of the spheroids, as this pattern has been observed repeatedly, and the DAPI staining confirms the presence of nuclei.

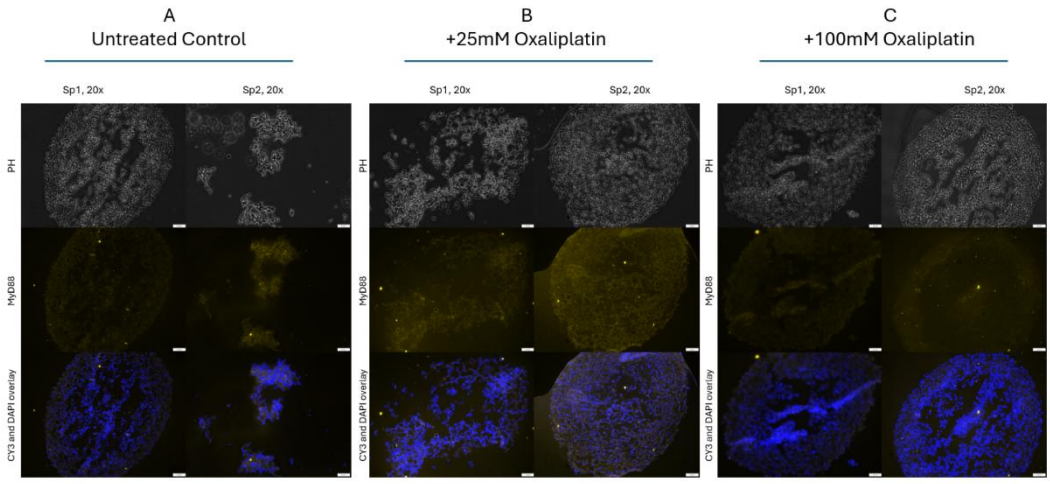

Figure 49 MyD88-Expression in Spheroid 1 and 2 of D7. *Representative images of untreated control spheroids (A) compared to spheroids treated with 25 mM (B) and 100 mM oxaliplatin (C), in 20x magnification (scale bar: 50 µm). Overall, the expression appears to be similarly distributed across the three blocks (A, B and C), showing few small yellow puncta across all CY3 panels. The blue color of the cell nuclei from the DAPI-staining is visible in the CY3+DAPI overlay.*

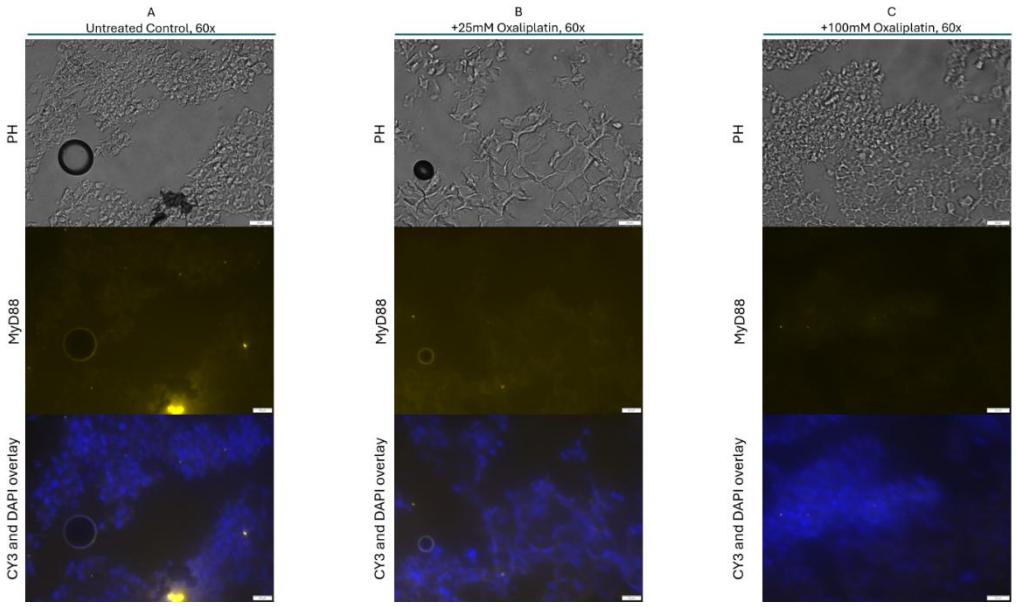

Figure 50 MyD88-Expression in the most representative spheroid of D7. *Representative images of untreated control spheroids (A) compared to spheroids treated with 25 mM (B) and 100 mM oxaliplatin (C), in 60x magnification (scale bar: 20 µm). Only one strong yellow signal in block A is visible, which seems to be an antibody aggregate. The blue color of the cell nuclei from the DAPI-staining is visible in the CY3+DAPI overlay.*

Here again (**Figure 51-Figure 52**) no control survived the staining, therefor no results are demonstrated. The results of MyD88 staining on spheroids from D8 again show the same pattern as observed on D7. Although the control group is missing, it is still clear that MyD88 does not exhibit homogeneous expression, regardless of whether the spheroid was treated with 25 mM or 100 mM.

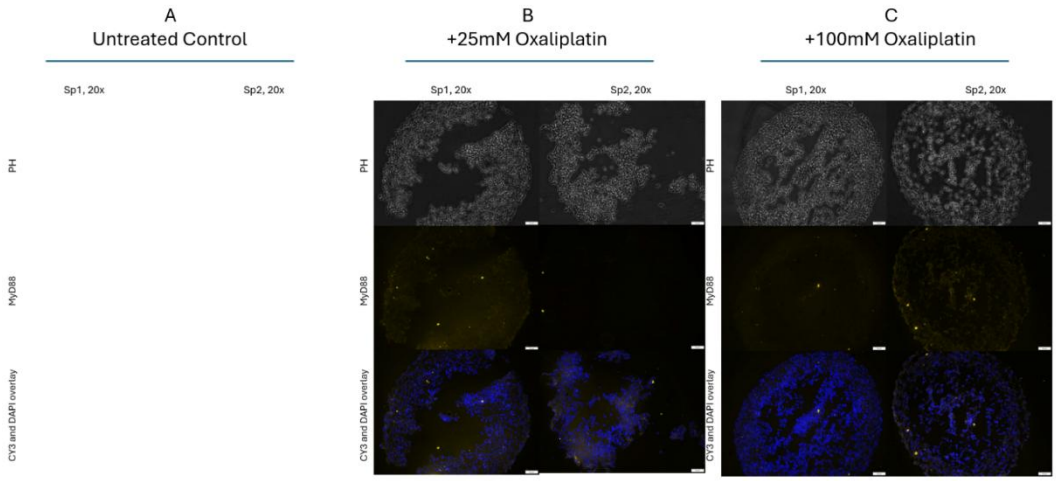

Figure 51 MyD88-Expression in Spheroid 1 and 2 of D8. *Representative images of untreated control spheroids (A) compared to spheroids treated with 25 mM (B) and 100 mM oxaliplatin (C), in 20x magnification (scale bar: 50 µm). It is important to note that Sp1 and Sp2 of block A were destroyed during the staining process, therefor no results can be shown. Overall, the expression appears to be similarly distributed across the last two blocks (B and C). Again, the yellow spots in the CY3 panels are heterogeneously distributed, very few and weak. The blue color of the cell nuclei from the DAPI-staining is visible in the CY3+DAPI overlay.*

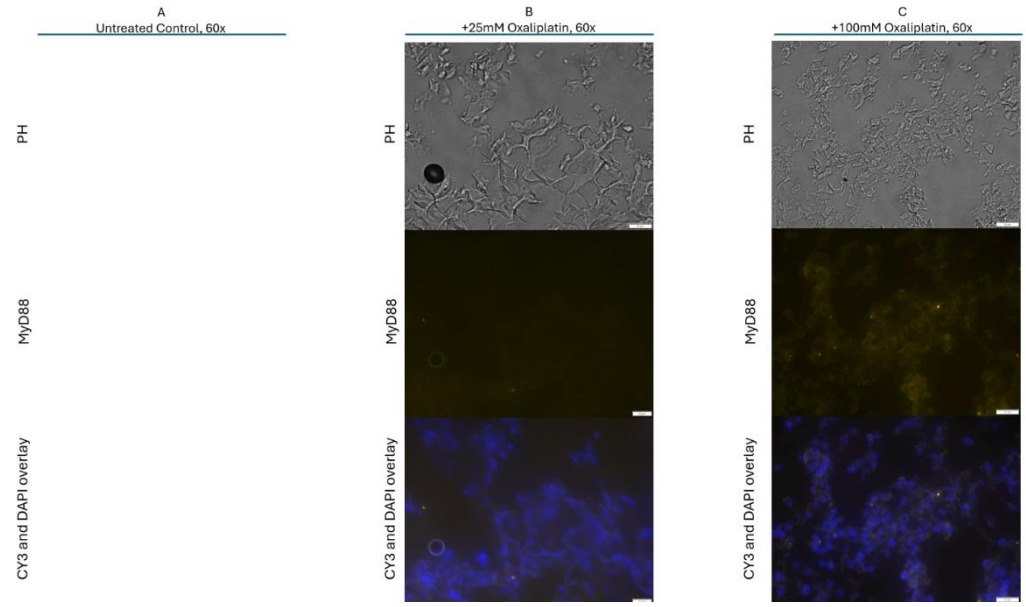

Figure 52 MyD88-Expression in the most representative spheroid of D8*. Representative images of untreated control spheroids (A) compared to spheroids treated with 25 mM (B) and 100 mM oxaliplatin (C), in 60x magnification (scale bar: 20 µm). It is important to note that Sp1 and Sp2 of block A were destroyed during the staining process, therefor no results can be shown. Across block B and C the CY3 panels lack any yellow stain, the only visible yellow stain in block C is what seems to be background. The blue color of the cell nuclei from the DAPI-staining is visible in the CY3+DAPI overlay.*

8 Conclusion

The primary objective of this study was to investigate the effect of oxaliplatin on TLR4 signaling pathways in colorectal cancer using both in vivo and in vitro models. Specifically, the expression and localization of key signaling proteins—NFkB, TRAM1, and MyD88—were analyzed in order to determine whether oxaliplatin influences inflammatory signaling pathways associated with tumor progression. While assessing the effect of oxaliplatin was the main goal, an additional important objective was to examine the baseline expression of these three targets in healthy, tumor, and transitional tissue regions in non-oxaliplatin-treated mice and subsequently compare these patterns to those observed under oxaliplatin treatment.

A central finding of this work is that oxaliplatin treatment did not result in any clear or consistent modulation of TLR4-associated signaling components in the analyzed samples. Across both mouse-derived tissues and spheroid models, the expression patterns of NFkB, TRAM1, and MyD88 remained largely unchanged when comparing treated and untreated groups. This suggests that, under the experimental conditions applied in this study, oxaliplatin does not significantly alter TLR4 signaling at the protein expression level.

The analysis of NFkB expression revealed generally weak and highly localized signals, particularly within tumor tissues. While some expression was observed in healthy and transitional tissue regions, tumor nodules exhibited minimal activation. Furthermore, the observed staining pattern was often punctate and inconsistent, raising the possibility of non-specific antibody binding or insufficient signal amplification. Additionally, no clear nuclear localization of NFkB was detected. This indicates that NFkB was either not activated or only partially activated in the samples examined.

TRAM1 expression showed a markedly different pattern. In all analyzed samples, TRAM1 was consistently absent in tumor regions but strongly expressed in healthy pancreatic tissue. This observation suggests a potential downregulation of TRAM1 in tumor cells, which may indicate a shift in TLR4

signaling dynamics during tumorigenesis. However, similar to NFkB, no differences between oxaliplatin-treated and untreated groups were observed. This implies that TRAM1 expression is not directly influenced by oxaliplatin under the conditions tested, or that any potential effects occur at a level not detectable by the employed methods.

MyD88 expression was overall very weak and largely indistinguishable from background staining. The absence of clear expression patterns makes it difficult to draw definitive conclusions regarding its role in this context. It is possible that MyD88 is expressed at low levels in the analyzed tissues or that the antibody sensitivity was insufficient. Additionally, the small sample size may have contributed to the lack of detectable differences. Given the importance of MyD88 as a central adapter protein in TLR4 signaling, further investigation using more sensitive techniques would be highly valuable.

Another important aspect of this study is the use of both in vivo and in vitro models. The CT26 mouse model provided a physiologically relevant system to study tumor growth and metastasis in an immunocompetent environment. However, variability between individual animals and the limited number of samples may have affected the robustness of the results. The use of 3D spheroid cultures represents a significant strength of this study, as these models better mimic the structural and functional properties of solid tumors compared to traditional 2D cultures. Nevertheless, similar to the in vivo findings, no significant treatment-related effects were observed in spheroids.

Despite these limitations, this study provides valuable insights into the relationship between oxaliplatin treatment and TLR4 signaling in colorectal cancer. The lack of observable effects suggests that the interaction between chemotherapy and immune signaling pathways is more complex than previously assumed. It is possible that oxaliplatin influences TLR4 signaling indirectly or at different time points not captured in this study. Alternatively, its effects may be more pronounced at the level of gene expression or post-translational modifications rather than protein abundance.

Future research should focus on expanding the sample size and incorporating additional analytical techniques. Moreover, investigating additional

components of the TLR4 pathway, including upstream receptors and downstream cytokines, could offer a more comprehensive understanding of the signaling network.

In conclusion, this study demonstrates that oxaliplatin does not significantly alter the expression of key TLR4 signaling proteins in the analyzed colorectal cancer models. While this finding may appear negative, it highlights the complexity of tumor-immune interactions and underscores the need for more comprehensive and quantitative approaches in future research. Understanding the interplay between chemotherapy and immune signaling remains a critical step towards the development of more effective and targeted cancer therapies.

9 References

Alexandra Fauvre, C. U.-A.-V. (2025). Oxaliplatin, ATR inhibitor and anti-PD-1 antibody combination therapy controls colon carcinoma growth, induces local and systemic changes in the immune compartment, and protects against tumor rechallenge in mice. *J Immunother Cancer*, 1-2.

Amina M. Illias, K.-J. Y.-H. (2022). Dorsal root ganglion toll-like receptor 4 signaling contributes to oxaliplatin-induced peripheral neuropathy. *Pain*, 1-2.

Ana S. Nunes, A. S. (2018). 3D tumor spheroids as in vitro models to mimic in vivo human solid tumors resistance to therapeutic drugs. *pubmed*, 206-207.

Anderson, J. (2025). *leica*. Retrieved from https://www.leicabiosystems.com/en-at/knowledge-pathway/immunohistochemistry-an-overview-steps-to-better-ihc-staining/

Anna Stierschneider, C. W. (2023, November 24). Shedding light on the molecular and regulatory mechanisms of TLR4 signaling in endothelial cells under physiological and inflamed conditions. *Front Immunol*, 2-3. Retrieved from frontiers in immunology: https://www.frontiersin.org/journals/immunology/articles/10.3389/fimmu.2023.1264889/full

Chandra Sekhar Singh, S. R. (2015). EVALUATION OF ANTIDIABETIC ACTIVITY OF AN IMPORTANT MEDICINAL PLANT ALOE CIM-SHEETAL LEAF EXTRACT. *INTERNATIONAL JOURNAL OF BIOASSAYS*, 3997.

Clauberg Sigrid. (2011). *Subzelluläre Lokalisation des endogenen Proteins vor und nach Inkubation mit spezifischen Toll-like Rezeptor-Liganden.* Düsseldorf: Heinrich-Heine-Universität.

Diana Groza, S. G. (2018). Bacterial ghosts as adjuvant to oxaliplatin chemotherapy in colorectal carcinomatosis. *Oncoimmunology*, 12.

Florian Wirsdörfer, V. J. (2017, August). Modeling DNA damage-induced pneumopathy in mice: insight from danger signaling cascades . *Radiat Oncol*, 142. Retrieved from https://www.researchgate.net/figure/Schematic-illustration-of-DAMP-TLR-inflammasome-interactions-Damage-induced-release-of_fig2_319274410

Franziska Beuing. (2022). *Die Bedeutung des Hypoxie-induzierbaren Faktors (HIF) – 1α für den Verlauf einer akuten Infektion mit murinem Zytomegalievirus (MCMV).* Essen: Universität Duisburg-Essen.

Hitoshi Ozawa. (2019). Principles and basics of immunohistochemistry. *Nihon Yakurigaku Zasshi*, 156-164.

J. M. Woynarowski, S. F. (2000, July 11). Oxaliplatin-induced damage of cellular DNA . *Mol Pharmacol*, 2. Retrieved from https://www.researchgate.net/figure/The-structures-of-oxaliplatin-and-cisplatin_fig1_12284495

Jäger Doreen. (2014, 7 11). *Elektronische Hochschulschrifeten der LMU München.* München: Medizinischen Fakultät Ludwig-Maximilians-Universität. Retrieved from https://edoc.ub.uni-muenchen.de/17349/1/Jaeger_Doreen.pdf

Jesus C. Fabregas, B. R. (2022). Clinical Updates for Colon Cancer Care in 2022. *Clin Colorectal Cancer*, 198-203.

John K. C. (2014). The wonderful colors of the hematoxylin-eosin stain in diagnostic surgical pathology. *Int J Surg Pathol*, 12-32.

Josephine Dubois, G. S. (2021). The human TRAM1 locus expresses circular RNAs. *Sci Rep*, 1-2.

Lucas G. A. Ferreira, F. A. (2022). Epididymal embryonic development harbors TLR4/NFKB signaling pathway as a morphogenetic player. *J Reprod Immunol*, 2-3.

Luke A. J. O'Neill, K. A. (2003). The Toll-IL-1 receptor adaptor family grows to five members. *Trends Immunol*, 286.

Melissa Eilbes. (2025). *bioRender*. Retrieved from https://www.biorender.com/template/immunohistochemistry-ihc

Nelleke P. M. Brouwer, A. C. (2018). An overview of 25 years of incidence, treatment and outcome of colorectal cancer patients. *Int J Cancer*, 2758-2766.

Nikolay N. Kuzmich, K. V.-L. (2017). TLR4 Signaling Pathway Modulators as Potential Therapeutics in Inflammation and Sepsis. *pubmed*, 2-3.

Ping Fan a, J.-J. Z.-Q.-X.-Y.-H.-S. (2012). Hypoxia-inducible factor-1 up-regulates the expression of Toll-like receptor 4 in pancreatic cancer cells under hypoxic conditions. *pubmed*, 1.

Sambrook J., F. E. (1989, 4). *Molecular cloning: a laboratory manual.* New York: Cold spring harbor laboratory press. Retrieved from sigmaaldrich: https://www.sigmaaldrich.com/AT/de/technical-documents/technical-article/genomics/nucleic-acid-labeling-and-detection/detection-methods?srsltid=AfmBOopNqYRhXSSitIyDHxbPvXyd_bSzyuKfa4T1vuw8vqpdRIWpNp6Z

Sandeep Rajput, L. D.-D. (2013). TLR4 is a novel determinant of the response to paclitaxel in breast cancer. *Mol Cancer Ther*, 1676-1687.

Shengwei Han, W. X. (2016). Crosstalk between the HIF-1 and Toll-like receptor/nuclear factor-κB pathways in the oral squamous cell carcinoma microenvironment. *pubmed*, 37773.

Sun, Z. L. (2022). Downregulated TICAM1 is a prognostic biomarker and associated with immune tolerance of Wilms tumor patients. *pubmed*, 1-9.

Taro Kawai, S. A. (2010). The role of pattern-recognition receptorsin innate immunity: update on Toll-likereceptors. *Nat Immunol*, 373-374.

Thai Tra Dang, V. N. (2025). TLR4/MyD88 expression patterns and novel genetic variants: association with aggressive clinicopathological features in colorectal cancer. *pubmed*, 1-15.

Ti Ngoc Le. (2020). Investigating tumor-microbe interaction in cell spheroids of murine breast cancer and in tissue samples. 11-12.

Ting-Ting Li, S. O. (2014). Toll-like receptor signaling in colorectal cancer. *pubmed*, 1-5.

Vanesa Stojanovska, R. M. (2018). Oxaliplatin-induced changes in microbiota,TLR4+ cells and enhanced HMGB1 expression. *pubmed*, 1-31.

Worawat Songjang, C. N. (2022). Tumor-Promoting Activity and Proteomic Profiling of Cisplatin/Oxaliplatin-Derived DAMPs in Cholangiocarcinoma Cells. *pubmed*, 1-8.

Xiao YANG, G. T. (2018). TLR4 promotes the expression of HIF-1α by triggering reactive oxygen species in cervical cancer cells in vitro-implications for therapeutic intervention. *pubmed*, 2229-2230.

Yoon Hee Chung, D. K. (2016). Enhanced TLR4 Expression on Colon Cancer Cells After Chemotherapy Promotes Cell Survival and Epithelial–Mesenchymal Transition Through Phosphorylation of GSK3β. *Anticancer Res*, 1-13.

10 List of Figures

11 List of Tables